AD-A258 802

HIGH STRAIN-RATE COMPRESSION TESTING OF A CERAMIC MATRIX COMPOSITE

Accession For
NTIS GRA&I ☑
DTIC TAB ☐
Unannounced ☐
Justification
By
Distribution/
Availability Codes
Dist | Avail and/or Special
A-1

by

James M. Parker

DTIC QUALITY INSPECTED 2

A thesis submitted to the Faculty of the University of Delaware in partial fulfillment of the requirements for the degree of Master of Material Science and Engineering in Materials Science

December 1992

Copyright 1992 James M. Parker
All Rights Reserved

92-30703

10P8

92 1 9

SECURITY CLASSIFICATION OF THIS PAGE

REPORT DOCUMENTATION PAGE

Form Approved OMB No 0704-0188 Exp Date Jun 30 1986

(2)

1a REPORT SECURITY CLASSIFICATION: U

1b RESTRICTIVE MARKINGS

2a SECURITY CLASSIFICATION AUTHORITY

3 DISTRIBUTION/AVAILABILITY OF REPORT: Unlimited

2b DECLASSIFICATION/DOWNGRADING SCHEDULE

4 PERFORMING ORGANIZATION REPORT NUMBER(S)

5 MONITORING ORGANIZATION REPORT NUMBER(S)

DTIC ELECTE DEC 3 1992 S C D

6a NAME OF PERFORMING ORGANIZATION: CPT James M. Parker, US Army

6b OFFICE SYMBOL (If applicable)

7a NAME OF MONITORING ORGANIZATION

6c ADDRESS (City, State, and ZIP Code): 8 Wellington Dr. Newark, DE 19702

7b ADDRESS (City, State, and ZIP Code)

8a NAME OF FUNDING/SPONSORING ORGANIZATION: US Army (USASD) Student Detachment

8b OFFICE SYMBOL (If applicable): ATZI-TBD

9 PROCUREMENT INSTRUMENT IDENTIFICATION NUMBER

8c ADDRESS (City, State and ZIP Code): FT. Benjamin Harrison, IN 46216-5820

10 SOURCE OF FUNDING NUMBERS

PROGRAM ELEMENT NO	PROJECT NO	TASK NO	WORK UNIT ACCESSION NO

11 TITLE (Include Security Classification): High Strain-rate Compression Testing of a Ceramic Matrix Composite

12 PERSONAL AUTHOR(S): CPT James M. Parker

13a TYPE OF REPORT	13b TIME COVERED	14 DATE OF REPORT (Year, Month, Day)	15 PAGE COUNT
THESIS	FROM SEP 90 TO DEC 92	1 DEC 92	100

16 SUPPLEMENTARY NOTATION: Master's Thesis - University of Delaware by CPT James M. Parker U.S. Army

COSATI CODES		
FIELD	GROUP	SUB-GROUP

17 SUBJECT TERMS (Continue on reverse if necessary and identify by block number): Composite, Ceramic, High strain-rate, Compression Testing, Split-Hopkinson Pressure Bar, Particle Reinforcement, Aluminum Oxide, Silicon Carbide

19 ABSTRACT (Continue on reverse if necessary and identify by block number)

A particle reinforced ceramic matrix composite was compression tested at high strain rates to examine its behavior under increasing, high strain rates. The composite was manufactured by the Lanxide® Dimox™ melt oxidation process and consisted of an Al_2O_3/Al matrix with SiC particulate reinforcement. The high strain-rate testing was conducted using a Split-Hopkinson Pressure Bar. The composite was tested at four mean strain rate ranges from 38.3 /sec. to 291.3 /sec. From the test data ultimate stresses, strains, and strain rates were calculated. Optical and scanning electron microscopy were performed on both fractured and whole specimens. Additional low strain-rate compression testing was performed at strain rates of 3.509 /sec. and .351 /sec.

20 DISTRIBUTION/AVAILABILITY OF ABSTRACT: ☒ UNCLASSIFIED UNLIMITED ☐ SAME AS RPT ☐ DTIC USERS

21 ABSTRACT SECURITY CLASSIFICATION: U

22a NAME OF RESPONSIBLE INDIVIDUAL: CPT James M. Parker

22b TELEPHONE (Include Area Code): (302) 836-6008

22c OFFICE SYMBOL

DD FORM 1473, 84 MAR — 83 APR edition may be used until exhausted. All other editions are obsolete.

SECURITY CLASSIFICATION OF THIS PAGE

ACKNOWLEDGEMENTS

Were it not for Dr. Ian W. Hall, I would not be writing this page. He was instrumental in providing me an opportunity to learn a discipline that I would never have known otherwise. His knowledge, support, patience, and humor have, thankfully, been boundless and greatly appreciated. I am in debt to him for all that he has done for me.

I would also like to express my gratitude to Jim Adkins, Art Baeckel, Linda Clifton, Touy Thiravong, Dr. Ralf Tschirshnitz, Bob Weiland, and Roger Williams for their hands-on help in every aspect of the testing and analysis.

Finally, you can't have a dance without music and for this dance, the music, in the form of their ceramic composite, was kindly donated by the Lanxide® Corporation.

TABLE OF CONTENTS

LIST OF FIGURES v
LIST OF TABLES vii
ABSTRACT viii

Chapter

1 INTRODUCTION 1
2 HIGH STRAIN-RATE COMPRESSION TESTING OF CERAMIC MATRIX COMPOSITES 3
3 DESCRIPTION OF LANXIDE® CERAMIC MATRIX COMPOSITE 8

3.1 Material Manufacturing Process 8
3.2 Material Properties 10

4 EXPERIMENTAL PROCEDURES 13

4.1 SHPB Theory 13
4.2 SHPB Specimen Manufacture 20
4.3 High Strain-rate Testing 23
4.4 Low Strain-rate Testing 24

5 RESULTS AND DISCUSSION 26

5.1 SHPB Results 26
5.2 Microscopy Analysis 37
5.3 Low Strain-rate Results 59

6 CONCLUSIONS 67

6.1 Conclusions 67
6.2 Suggestions for Further Research 70

Appendix

A SPLIT-HOPKINSON PRESSURE BAR OPERATING MANUAL . 71
B SHPB COMPUTER PROGRAM 89

REFERENCES 91

LIST OF FIGURES

Figure 3.1 DIMOX$_{TM}$ Process 9

Figure 4.1 SHPB Bar Arrangement 14

Figure 4.2 Nonlinear Wave Propagation in Transmitted Wave 18

Figure 4.3 University of Delaware SHPB 25

Figure 5.1 Typical SHPB Reflected and Transmitted Waves 27

Figure 5.2 68.95 kPa Times to Reach Ultimate Stress (μsec) 30

Figure 5.3 #1-68.95 kPa, Stress v. Strain 33

Figure 5.4 #5-137.9 kPa, Stress v. Strain 34

Figure 5.5 #3-206.85 kPa, Stress v. Strain . . . 35

Figure 5.6 #2-275.8 kPa, Stress v. Strain 36

Figure 5.7 Untested Specimen Microstructure (x40) 39

Figure 5.8 206.85 kPa Specimen Microstructure (x40) 40

Figure 5.9 Identification of Microstructure Phases (x40) 41

Figure 5.10 Aluminum Phase Spectrum 42

Figure 5.11 Aluminum Oxide Phase Spectrum 43

Figure 5.12 Copper-Aluminum Phase Spectrum 44

Figure 5.13 Pores in SiC Particles (x20) 46

Figure 5.14 Crack Branching and Deflection 47

Figure 5.15 Pore in 68.95 kPa Specimen 48

Figure 5.16 Pores in 206.85 kPa Specimen 49

Figure 5.17 Microcracking in SiC Particle 51

Figure 5.18 Microcrack from Pore 52

Figure 5.19 Fracture in SiC Particle 53

Figure 5.20 Aluminum Oxide Grains (x70,000) . . . 57

Figure 5.21 Random Dislocation Distribution in Al Grain Before Testing (x70,000) 58

Figure 5.22 Recrystallization in Aluminum Grain as a Result of Testing (x90,000) . . . 60

Figure 5.23 Aluminum Extruded into Crack (x140,000) 61

Figure 5.24 Plastic Deformation in SiC Particle (x90,000) 62

Figure 5.25 Low Strain-rate Stress v. Strain Curve 63

Figure 5.26 Mean Ultimate Stresses v. Mean Ultimate Strain Rates 66

LIST OF TABLES

Table 3.1 Mechanical Property Data 11

Table 3.2 Compressive Strength (MPa) 11

Table 3.3 Fracture Toughness ($MPa \cdot m^{1/2}$) 12

Table 5.1 Mean Ultimate Strain Rates 28

Table 5.2 Mean Ultimate Stress 31

Table 5.3 Mean Ultimate Strain 31

Table 5.4 Compressive Strengths of SiC and Al_2O_3 (GPa) 32

Table 5.5 Low Strain-rate Results (MPa) 64

ABSTRACT

A particle reinforced ceramic matrix composite was compression tested at high strain rates to examine its behavior under increasing, high strain rates. The composite was manufactured by the Lanxide® DIMOX™ melt oxidation process and consisted of an Al_2O_3/Al matrix with SiC particulate reinforcement. The high strain-rate testing was conducted using a Split-Hopkinson Pressure Bar. The composite was tested at four, mean strain rate ranges from 38.3 /sec. to 291.3 /sec. From the test data, ultimate stresses, strains, and strain rates were calculated along with elastic moduli. Optical and scanning microscopy were performed on both fractured and whole tested specimens. Additional low strain-rate compression testing was performed at strain rates of 3.509 /sec. and .351 /sec.

Chapter 1

INTRODUCTION

The utilization of ceramic matrix composites is growing as production costs decrease and new uses are found. Depending upon the use, the ceramic composite may be reinforced with either fibers, whiskers, or particles. One area where particulate reinforced ceramic composites, specifically, are well suited is in applications involving dynamic loading conditions such as tooling, mining applications, and ballistic armor. In general, little research has been conducted to characterize the response of ceramic composites to high strain rate, dynamic loading conditions. Some work has been done for fiber and whisker reinforced ceramics, but, to the author's knowledge, none has been done for particle reinforced ceramics [1].

The particulate reinforced ceramic composite used in this study has yet to be characterized with respect to its high strain-rate microstructural response and mechanical properties. The composite was manufactured by the Lanxide® Corporation using its patented DIMOX™ process.

The high strain-rate compression testing of the composite was conducted using a Split-Hopkinson Pressure Bar (SHPB) at strain rates up to ~$3x10^2$ /sec. Both fractured and whole specimens were examined using optical and electron microscopy to reveal the composite's microstructural response.

The results of this study will provide the first characterization of a particle reinforced ceramic composite in compression at high strain rates and the first high strain-rate characterization of a ceramic composite manufactured by the DIMOX™ process. This information will aid in material selection and provide some indication as to how to tailor the composite's constituents to the required performance needs.

High strain-rate compression testing of ceramic matrix composites is detailed in Chapter 2. Chapter 3 describes the DIMOX™ manufacturing process and provides some mechanical property data. Chapter 4 outlines the theory behind the SHPB, the manufacture of the test specimens, and descriptions of the high strain-rate and low strain-rate testing. The test results and microscopy analysis are presented in Chapter 5. Chapter 6 presents the conclusions of this thesis and suggestions for further research.

Chapter 2

HIGH STRAIN-RATE COMPRESSION TESTING OF CERAMIC MATRIX COMPOSITES

In general, little research has been done in the characterization of ceramic matrix composites at high strain rates. In fact, to the author's knowledge, the results from any high strain-rate compression testing of particle reinforced ceramic matrix composites have yet to be published.

Extensive research has been done by Lankford on the high strain-rate behavior of both monolithic ceramics, and whisker and fiber reinforced ceramic composites. Examining the compressive strengths of silicon carbide and aluminum oxide [2], at strain rates $\leq 10^2$ /sec., Lankford found a slight degree of strain rate sensitivity in aluminum oxide. In contrast, the silicon carbide was not strain rate sensitive. Lankford attributed the strain rate behavior of aluminum oxide to the subcritical growth of axial microcracks within localized, resolved tensile stress fields. Conversely, the strain rate insensitivity of silicon carbide was due to the absence of the axial

microcracks. At strain rates $\geq 10^3$ /sec. on the other hand, the compressive strengths of both materials increased and exhibited a high degree of strain rate sensitivity.

Utilizing the SHPB to examine the high strain-rate compressive strengths of SiC, Al_2O_3, and Si_3N_4 [3], Lankford, citing previous work by Kipp et al. [4], stated that microcrack growth rather than microcrack initiation was suppressed by material inertia at high strain rates. In other words, the ceramics continued to initiate cracks at high strain rates but the growth of the cracks was suppressed by the momentum of the ceramics' mass which resulted in the generation of significant strengthening. Lankford also proposed a relationship between the materials' compressive strengths and their respective strain rates at strain rates $\geq 10^2$ /sec.;

$$\sigma_c \propto \dot{\epsilon}^{0.3} \tag{2.1}$$

where σ_c is the compressive fracture stress and $\dot{\epsilon}$ is the strain rate.

Scanning electron microscopy of aluminum oxide, silicon carbide, and two forms of silicon nitride revealed [5] that the axially oriented microcracks were nucleated by twins and sharp-edged grain boundary voids. At strain rates $\leq 10^2$ /sec., compressive failure of the materials was controlled by the thermally activated growth of axially

oriented tensile microcracks. The identity of the thermally activated process was unknown.

Compression testing of a commercial 85% aluminum oxide with a glassy phase at strain rates between $.11 \times 10^{-3}$ /sec. and .81 /sec. [6] revealed that the aluminum oxide failed by granulation, and fracturing into small flakes and splinters with long dimensions parallel to the compression axis. The existence of the flakes and splinters was seen as evidence that the aluminum oxide failed by the growth of tensile microcracks in planes parallel to the compression axis. At the highest loading rate, the fragments were slickenslided (a smooth, often striated surface produced by movement along a fracture) and exhibited signs of either localized melting or plastic grooving which were induced by friction between adjacent, shearing flakes.

The objective of the research by Lankford and Blanchard [7] was to characterize the compressive strength and behavior of a 10 vol.% SiC whisker-reinforced Si_3N_4 composite. The material was tested at strain rates from 10^{-5} /sec. to 10^{3} /sec., with the SHPB used for the higher strain rates. From their results, Lankford and Blanchard concluded that the composite's high strain-rate behavior was governed by the effects of matrix microfracture and was not influenced by the presence of the whiskers. The

microfracture process was believed to be related to the existence of tensile enclaves of various strengths localized at grain boundaries.

Examining the dynamic compressive fracture of a pyroceramic matrix reinforced with 60 vol.% SiC fibers [8] Lankford showed that the material experienced increased strain-rate hardening when the failure mechanism was complex. This was achieved when the fiber reinforcement was parallel to the compression axis. The resulting failure mechanism was a combination of inertia-controlled microcrack accommodation of kink band nucleation and rate-dependent kink propagation. The kink propagation occurred at very high local strain rates which may have resulted in local heating during the shear process.

Additional high strain-rate ceramic material responses have been identified and examined. The adiabatic shearing described by Lankford in [6] and [8] has been defined as arising from the heat generated in localized bands which cannot be dissipated because of the strain rate and the thermal properties of the material [9]. This phenomenon has been noted elsewhere in explosively deformed alumina [10]. High strain-rate microstructural damage has also been attributed to a combination of differences in impedance between the material components of a multi-phase material and thermal

residual stresses arising from different coefficients of thermal expansion [11]. Additionally, the microstructural response of a specimen to the compressive and tensile reflected waves experienced in the SHPB has been further described [12]. Specifically, when a tensile wave encounters a crack or the interface between two phases in a ceramic having different impedances, reflection and transmission of the wave will alter the state of stress at the crack or interface. Flaws in the ceramic which are normal to the direction of propagation of the shock wave will tend to open up under the reflected tensile stress and microcracks will be generated at interphase boundaries in the same manner.

Chapter 3

DESCRIPTION OF LANXIDE® CERAMIC MATRIX COMPOSITE

3.1 Material Manufacturing Process

The tested ceramic matrix composite was manufactured using the patented Lanxide® DIMOX™ process [13-16]. The process is centered around the directed melt oxidation of a molten metal by a gaseous oxidant to form a ceramic reaction product (Figure 3.1). At the beginning of the process, the ceramic reaction product is formed at the interface between the molten metal and the oxidant. As the reaction product grows, the reaction progresses via the transport, through the ceramic reaction product, of molten metal to the molten metal-oxidant interface. Capillary action is the mechanism that moves the molten metal via microscopic channels in the reaction product. The process is completed when the quantities of the molten metal and/or the oxidant are exhausted. The morphology of the resulting ceramic is a three dimensionally

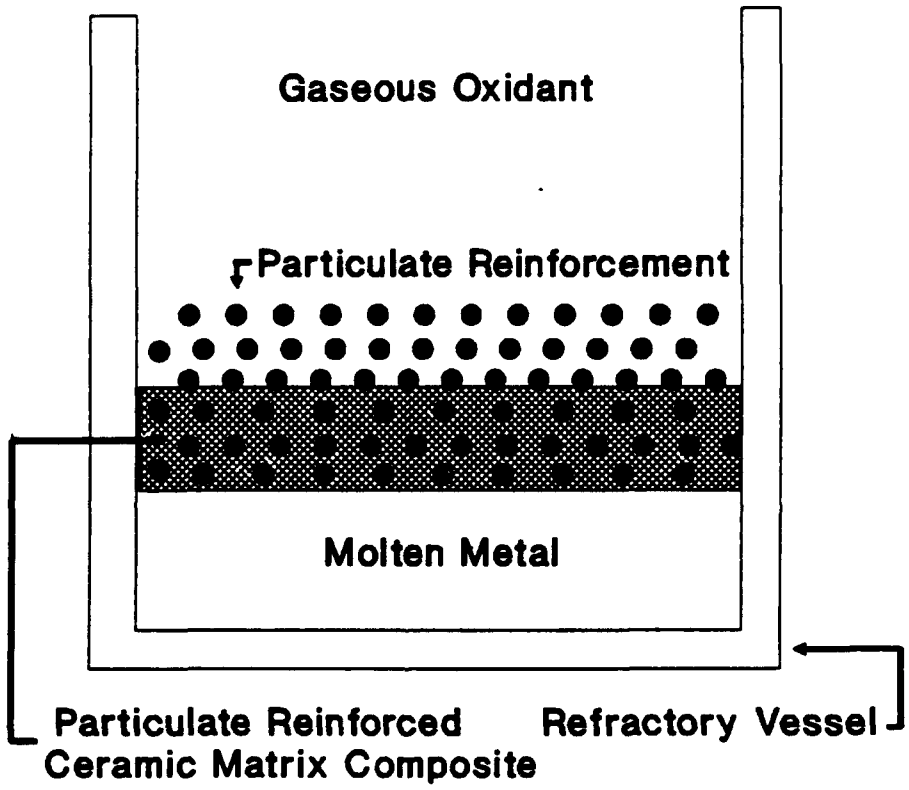

Figure 3.1 DIMOX™ Process.

interconnected ceramic phase with an interconnected ductile metallic phase of 5 to 30% by volume.

The kinetics of the reaction and the process parameters can be modified to tailor the reaction product's material properties to desired needs. Dopants of Mg and a Group IVA element (at up to a few weight percent) are introduced as constituents in the molten alloy to stimulate the oxidation process and prevent blocking of the capillary channels. The process temperature is selected from a narrow range of temperatures above the melting point of the metal alloy and below the melting point of the reaction product.

The reaction product can be reinforced with particles, whiskers, and fibers. A preforem of the reinforcement is shaped to the desired size and placed inside a mold. When the preform and metal alloy are heated to the selected process temperature and the other process conditions are met, the ceramic matrix grows around the reinforcement without displacing it. The result is an *in situ* composite of near-net shape.

3.2 Mechanical Properties

Published mechanical property data for a Lanxide® SiC_p reinforced Al_2O_3/Al matrix composite are shown in Table 3.1 [13].

Table 3.1 Mechanical Property Data.

Growth Temperature (°C)	Strength (MPa)	Fracture Toughness ($MPa \cdot m^{1/2}$)
900	350	7.8
1000	390	5.4
1150	525	4.7

The strength data are derived from room temperature 3-point bend tests.

Uniaxial compressive strengths of two, unreinforced Lanxide® Al_2O_3/Al composites are shown in Table 3.2 compared to a commercial alumina [14]. Composite I, with 22% aluminum, was grown at 1400 K and stopped before all of the molten aluminum had oxidized. Composite II, with 13% aluminum, was grown at 1600 K until all of the molten aluminum had oxidized. A sintered alumina, Durafrax® 1542, manufactured by Sohio Engineered Materials Co., was selected for the commercial alumina.

Table 3.2 Compressive Strength (MPa).

Composite I	Composite II	Durafrax® 1542
984±85	1901±190	2420±230

It was concluded that the difference in compressive strengths shown in Table 3.2 resulted from different degrees of connectivity between the aluminum phases in the composites. The aluminum in Composite II is almost totally surrounded (to the extent of creating inclusions) by alumina which acts to prevent the aluminum from shearing. In contrast, the aluminum in Composite I, containing about 50% more aluminum than Composite II, is not surrounded to the same degree by the alumina and is interconnected throughout the composite.

Fracture toughness data for Composites I and II, and Durafrax® 1542 are shown in Table 3.3 [14].

Table 3.3 Fracture Toughness ($MPa \cdot m^{1/2}$).

Composite I	Composite II	Durafrax® 1542
9.5	5.9	3.8

The impact of the volume percent of the aluminum on the fracture toughness is seen with Composite I having 22% aluminum, Composite II 13%, and Durafrax® 1542 0%. Aghajanian et al. [14] stated that the aluminum phase contributed to the work of fracture by absorbing a considerable amount of energy via crack bridging.

Chapter 4

EXPERIMENTAL PROCEDURES

4.1 SHPB Theory

The SHPB is one of the better known pieces of test apparatus for high strain-rate testing. First proposed, in a one bar configuration, by John and Bertram Hopkinson, the current two bar configuration was developed by Kolsky in 1948 [17].

As outlined by Zukas el al. [18] the heart of the SHPB is the striker bar which is accelerated by either a spring or a pressurized gas-gun. The accelerating striker bar impacts against the incident bar (Figure 4.1) and causes the creation of constant amplitude compressive pulses in both bars. The duration of the generated compressive pulse in the incident bar is twice the length of time for the wave to travel the striker bar. The magnitude of the compressive pulse is directly proportional to the velocity of the striker bar.

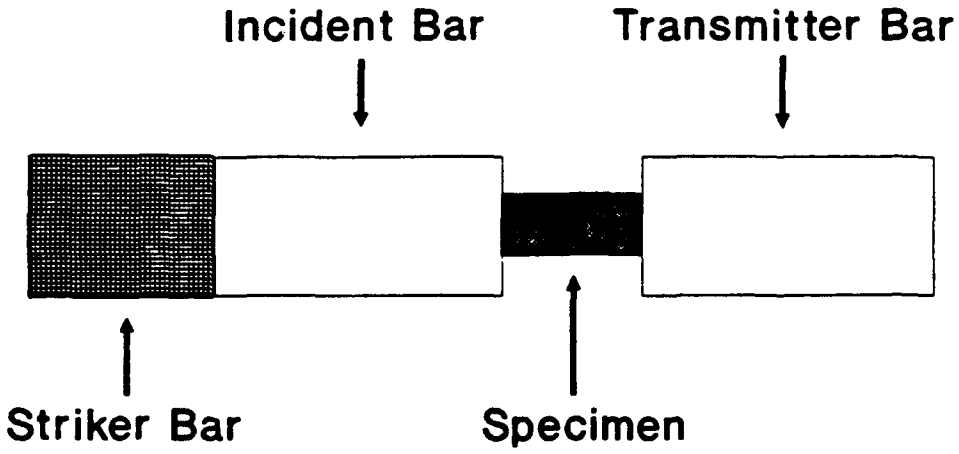

Figure 4.1 SHPB Bar Configuration.

Positioned at the opposite end of the incident bar is the specimen (Figure 4.1). When the compressive pulse in the incident bar reaches the specimen, a portion of the pulse is transmitted through the specimen into the transmitter bar and the remainder is reflected back into the incident bar. The partial transmission of the compressive pulse to the transmitter bar is the result of two factors; the difference in cross-sectional areas between the specimen and the larger incident and transmitter bars, and the difference in the acoustic impedances of the pressure bars and the specimen. The specimen's size and mechanical properties thus determine the shapes of the reflected and transmitted pulses.

Given that the striker, incident, and transmitter bars are of the same material and cross-sectional area, a set of relations for the specimen stress, strain, and strain rate can be derived;

$$\sigma_s = E\frac{A}{A_s}\epsilon_t \tag{4.1}$$

$$\epsilon_s = \frac{-2C_0}{L}\int_0^t \epsilon_r dt \tag{4.2}$$

$$\dot{\epsilon}_s = \frac{-2C_0}{L}\epsilon_r \tag{4.3}$$

where ϵ_s is the specimen strain, $\dot{\epsilon}_s$ is the specimen strain rate, σ_s is the specimen stress, ϵ_r is the reflected wave strain, ϵ_t is the transmitted wave strain, L is the specimen length, C_0 is the elastic wave velocity in the bars, A and A_s are the bar and specimen cross-sectional areas respectively, and E is the elastic modulus of the bars. These equations, based upon the earlier treatment by Zukas [18], are presented in Frey [19] and Choe [20].

Two assumptions govern the use of the equations. The first assumption is based upon the fact that the time it takes for the transmitted wave to travel the length of the specimen is small compared to the total time of the test. This enables many compressive and tensile wave reflections to occur within the specimen. These multiple reflections thus provide the basis for the assumption that the specimen stress and strain are uniform along the specimen. The second assumption is that the stresses and wave velocities at the ends of the specimen are transmitted without any dispersion along the incident and transmitter bars.

To detect the reflected and transmitted waves, strain gages are placed on the incident and transmitter bars equidistant from the specimen interface. This ensures that the reflected and transmitted waves arrive at the strain gages simultaneously.

The time it takes for a wave pulse to travel the length of the striker bar is a characteristic of each SHPB apparatus. The yield and ultimate stress points must occur within the wave pulse time window of the machine in order for them to be considered valid. For the University of Delaware SHPB, the yield and/or ultimate points must occur within 290 microseconds from the start of the test.

According to Zukas [18] and Rand [21] a major limitation in the use of the SHPB is the existence of nonlinear wave propagation in the specimen. The nonlinearity results from stress-wave reflections, stress nonuniformities, and large variations in the strain rate during the initial portions of the test. These effects are seen in region 1 of a typical transmitted wave shown in Figure 4.2. It is only when the curve smoothes out in region 2 that valid stress, strain, and strain rate values can be calculated. Rand estimated the size of region 1 to be twice the rise time of the incident pulse. Zukas and Rand both concluded that accurate information from the tested material's elastic region i.e., yield stress, strain, strain rate, and elastic modulus, could not be obtained.

Two phenomena, which can affect the accuracy of the SHPB test results, have also been identified with the

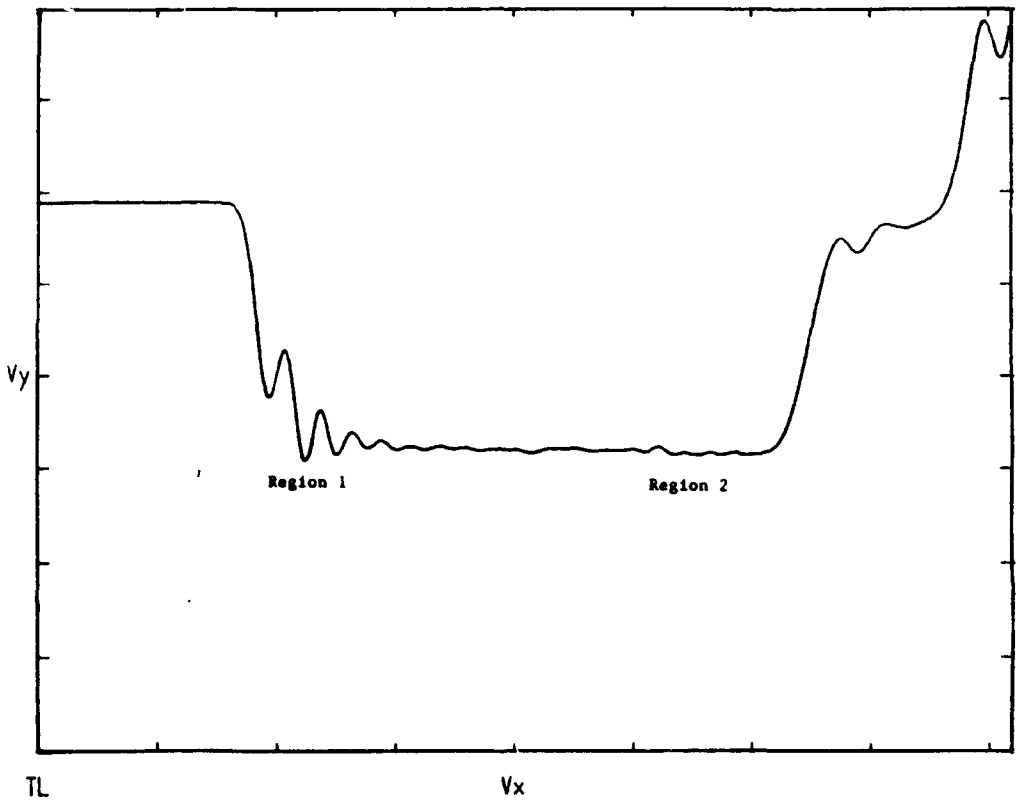

Figure 4.2 Nonlinear Wave Propagation in Transmitted Wave.

use of the compression version of the SHPB. Lindholm and Yeakley [22] have concluded that these effects could lead to measured stresses that are higher than the actual stresses and could be interpreted as resulting from a strain-rate effect.

The first effect concerns the stresses resulting from friction between the specimen ends and the ends of the bars. According to Gorham et al. [23] friction islikely to cause the most significant deviation from the assumptions of uniaxial and uniform stress within the specimen, and also cause large errors in the measured stresses. It was first suggested by Lindholm [24] to coat the specimen ends with molybdenum disulfide powder to minimize the effects of friction.

The second effect is most evident in ductile materials and occurs when the specimen is impacted, expands radially i.e. barrels, and experiences nonuniaxial strains. To achieve nearly uniaxial strain conditions, a tightly fitting collar has been utilized to restrain the radial motion [8]. However, it is difficult to achieve perfectly uniaxial strain conditions because a perfect fit between the collar and the specimen is difficult to attain and the collar, if it is made of an elastic material, may itself expand radially due to the force exerted by the specimen's radial expansion. Additionally, the attainment

of perfectly uniaxial strain may make the specimen stronger than the incident and transmitter bars.

An outline of the procedure for using the SHPB begins by lubricating the specimen with molybdenum disulfide powder and placing it between the incident and transmitter bars. The pressures of the inner and outer chambers of the gas-gun are then set. When the strain gages and oscilloscope are ready, the gas pressure in the inner chamber (which is higher than the outer chamber's pressure) is released causing the pressurized outer chamber gas to propel the striker bar through a barrel and impact the incident bar. The velocity of the striker bar and the resulting strain rate are, in general, determined by the pressure of the outer chamber, i.e., an increase in the outer chamber pressure increases the striker bar velocity and the strain rate. Specimens in this work were tested at four outer chamber pressures ranging from 68.95 kPa to 275.8 kPa.

4.2 SHPB Specimen Manufacture

The test specimens were manufactured from hexagonal tiles of Lanxide®'s 1090 ceramic armor. The hexagonal shaped tiles were 101.6 mm in diameter and 14.286 mm in thickness. Manufacture of the specimens began by cutting slices 12.065 mm thick, with two, parallel cut faces from the tile using a surface grinder

with a water-cooled diamond cutting wheel. Due to the composition of the material, each cut took approximately 40 minutes, hence the cutting of all of the slices at one time became impractical.

Ensuring that a face cut at an earlier time was parallel to a subsequent cut was critical to achieving ideal test conditions and results. Initially, faces cut at different times were deemed parallel when the tile face that was cut earlier was placed flat against the side of the cutting wheel. The cutting wheel was then adjusted, using Vernier calipers accurate to .025 mm, a distance 12.065 mm perpendicular to the cut face and a cut made. Subsequent measurement of the slices showed variations in width of up to .254 mm from end to end.

The non-parallelism seen in earlier slices was attributed to either the tile not being placed evenly against the cutting wheel and/or deflection in the cutting wheel caused by the tile placing too much force on one edge of the wheel. A method for producing truer slices was implemented near the end of the SHPB testing and was used for the specimens tested at an outer chamber pressure of 68.95 kPa. The modified method consisted of making a thin cut along an already cut face to true the tile to the cutting wheel. The cutting wheel was then shifted 12.065 mm and a cut made. A slice produced by this method was

used for the specimens tested at 68.95 kPa. These specimens varied in length from 12.167 to 12.294 mm.

The specimen diameter was created by a 9.525 mm outside diameter, diamond core drill. The slices were mounted with wax, cut face up, onto a steel backing plate which was placed in a Bridgeport mill. Using a speed of 400rpm (recommended by Lanxide®), the cylindrical specimens were cored from the slices using a core drill (Starlite Inc., part #101095) mounted in a water jacket to provide water as a coolant for the drilling. In initially becoming familiar with the manufacture of the specimens and the operation of the SHPB, a 7.939 mm outside diameter core drill was used. The smaller specimen produced by this core drill was found to fracture easily at 68.95 kPa so it was not possible to provide a testable range of strain rates; therefore, the change was made to the 9.525 mm core drill. The 9.525 mm core drill, used initially to test the suitability of the larger specimen, produced sample specimens with a diameter of 8.052 mm. This was the diameter finally selected for the specimen length in order to achieve the chosen length to diameter ratio of 1.5. New core drills, from the same manufacturer, used to core the actual test specimens, produced specimens that had a diameter of 8.255 mm. As slices 12.065 mm in width had already been made, it was decided to maintain the

specimen length at 12.065 mm and not strictly adhere to the length to diameter ratio.

Drilling the specimens took between 15 minutes and an hour each. The differences in drilling times are believed to be a function of the newness of the core drill and the pressure placed on the core drill. Light hand pressure was applied to the core drill as it cut through the material. In spite of the minimal pressure, the core drill tips would begin to flare before they fractured. Fracture occurred at the diamond impregnated tip after drilling about 10 specimens.

It was noted that the cored specimens normally were not cleanly cut through at the face of the slice mounted on the wax. As the core drill came closer to the face of the slice the force applied to core drill is thought to have caused the breakout of the material at the face. The breakout was never completely eliminated but was minimized by easing off on the pressure on the core drill as it neared the end of its cut and by having a measurably thick layer of wax between the slice and the steel.

4.3 High Strain-rate Testing

The high strain-rate testing was conducted on the Split-Hopkinson Pressure Bar at the University of Delaware. To test the material's response over a range of

strain rates, six specimens were tested at four pressures; 86.95, 137.9, 206.85, and 275.8 kPa. The pressure in the outer chamber of the SHPB was the independent test variable that caused the strain rate ranges to increase or decrease. An increase in the outer chamber pressure caused an increase in the striker bar velocities which in turn caused an increase in the range of strain rates experienced by the specimen. A detailed description of the operation of the University of Delaware SHPB is presented in Appendix A. Figure 4.3 is a diagram of the University of Delaware SHPB.

4.4 Low Strain-rate Testing

Six SHPB specimens were tested at low strain rates on an Instron hydraulic test machine. Three specimens were tested at a strain rate of 3.509 /sec. and the remaining three specimens at a strain rate of .351 /sec. The specimens were loaded until fracture occurred. The live output from the Instron was received by an X-Y printer which produced a graph of load versus time. The ultimate compressive strength of each specimen was then calculated from each graph.

Split Hopkinson Pressure Bar Apparatus.

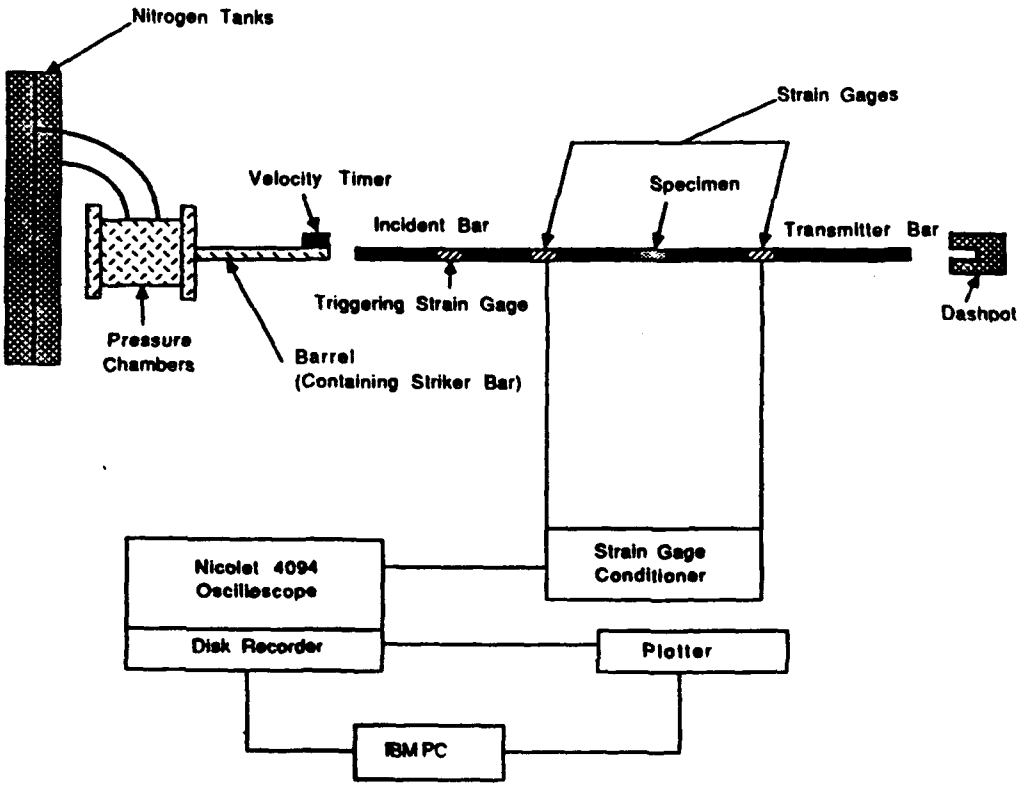

Figure 4.3 University of Delaware SHPB.

Chapter 5

RESULTS AND DISCUSSION

5.1 SHPB Results

Six specimens each were tested at four SHPB pressures. A typical set of recorded waves is shown in Figure 5.1. The upper curve is the transmitted wave and the lower curve is the reflected wave. The waves are recorded by the oscilloscope as voltages versus time. Figure 5.1 also shows where the ultimate strength point on the upper, transmitted curve was calculated. The ultimate point was defined as the minimum point along the smooth, uniform stress/strain region of the transmitted wave. A detailed description of the SHPB data analysis is given in Appendix A.

When tested, not all of the specimens fractured. The number of whole specimens decreased from four for the 68.95 kPa group to one for the 275.8 kPa group. Among the specimens that did fracture, a large number of long, axially-oriented fragments were observed throughout the

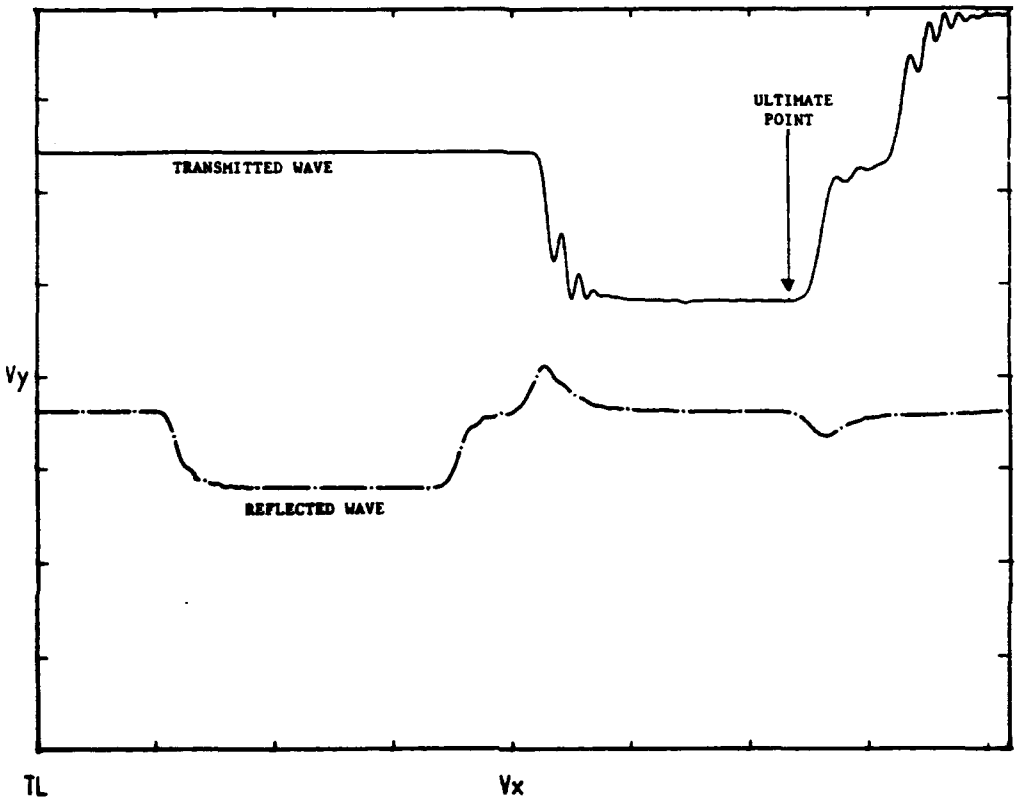

Figure 5.1 Typical SHPB Reflected and Transmitted Waves.

strain rates. It was also noted that the fragments changed from a few large chunks or slivers for the 68.95 kPa specimens to a large number of granules and powder with smaller slivers for the 275.8 kPa specimens.

The strain rates at the ultimate point ranged from a low of 29.51 /sec. to 326.84 /sec. over the range of outer chamber pressures. In general, the strain rate ranges at the ultimate point increased as the SHPB pressure increased. Table 5.1 lists the outer chamber pressures and their corresponding mean ultimate strain rates and standard deviations. Strain rates that were abnormally high or low for a given outer chamber pressure were discarded. These anomalies are thought to be caused by specimens that were manufactured with ends that were not parallel.

Table 5.1 Mean Ultimate Strain Rates.

Outer Chamber Pressure (kPa)	Mean Strain Rate (/sec.)	Standard Deviation (/sec.)
275.8	291.27	35.7
206.85	210.75	62.86
137.9	104.49	82.11
68.95	52.38	21.78

An examination of the relationship between the ultimate strain rates and the times at which the ultimate points occurred showed that, in general, the strain rates within a pressure group varied inversely in ultimate point time. Figure 5.2 shows the ultimate strain rates for the specimens tested at 68.95 kPa and lists their respective ultimate times in microseconds. The inverse relationship depicted in Figure 5.2 is expected because the ultimate strain rates are average strain rates which decrease over time.

The ultimate stress data shown in Table 5.2 shows the same general correlation between testing pressure and ultimate stress with the mean ultimate stress increasing as the SHPB pressure and ultimate strain rate increased. The lowest ultimate stress recorded was .814 GPa and the highest was 1.947 GPa. There is no correlation between the behavior of the ultimate stress curves with respect to whether the specimen fractured, nor with respect to the specimen's ultimate strain rate.

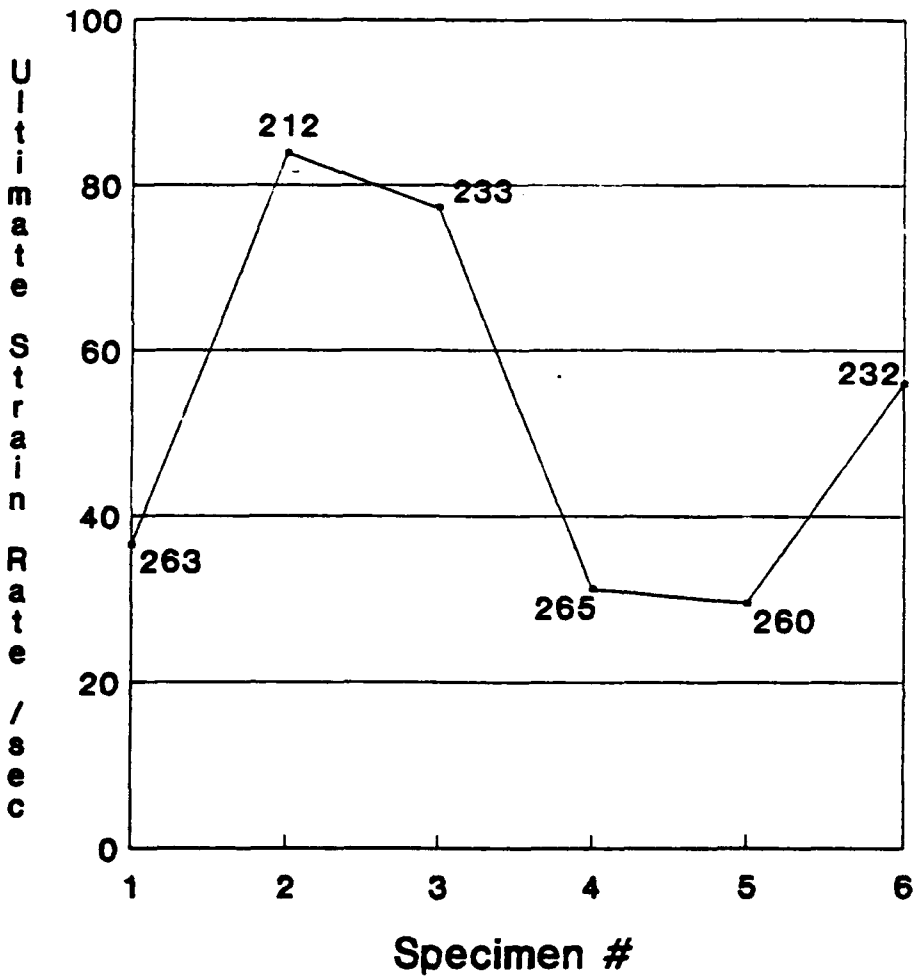

Figure 5.2 68.95 kPa Times to Reach Ultimate Stress (μsec).

Table 5.2 Mean Ultimate Stress.

Outer Chamber Pressure (kPa)	Mean Ultimate Stress (GPa)	Standard Deviation (GPa)
275.8	1.625	.200
206.85	1.431	.124
137.9	1.185	.095
68.95	.913	.072

The mean ultimate strains, as shown in Table 5.3, also increased as SHPB pressure increased. The smallest strain recorded was .00767% and the largest was .0297%.

Table 5.3 Mean Ultimate Strain.

Outer Chamber Pressure (kPa)	Mean Ultimate Strain (%)	Standard Deviation (%)
275.8	.0189	.0025
206.85	.0181	.0033
137.9	.0156	.0049
68.95	.0124	.0042

Similar strain-rate hardening results were reported by Lankford [2] for monolithic aluminum oxide and silicon carbide. Table 5.4 shows the fracture stresses of monolithic silicon carbide and aluminum oxide at a strain rate of ~10^3 /sec. The differences between the results

reported here and Lankford's are thought to be due to the existence of aluminum in the composite's matrix.

Table 5.4 Compressive Strengths of SiC and Al_2O_3 (GPa).

Al_2O_3	SiC
3.7	5.5

Figures 5.3 through 5.6 show representative stress v. strain curves for the four pressure groups. Each of the curves clearly show the effect of non-uniform wave propagation at the specimen/transmitter bar interface.

The curves were produced by multiplying the voltages at corresponding times from the transmitted and integrated reflected curves by the stress and strain calibration constants, respectively. The calibration constants are calculated during the SHPB test data analysis described in Appendix A.

In conducting the SHPB tests, it was noted that the surfaces of the removable stubs at the ends of the incident and transmitter bars occasionally required refinishing; typically this was necessary after every three tests at 275.8 kPa. The refinishing was required because the faces of the stubs became indented by the specimens and because debris from the test would become

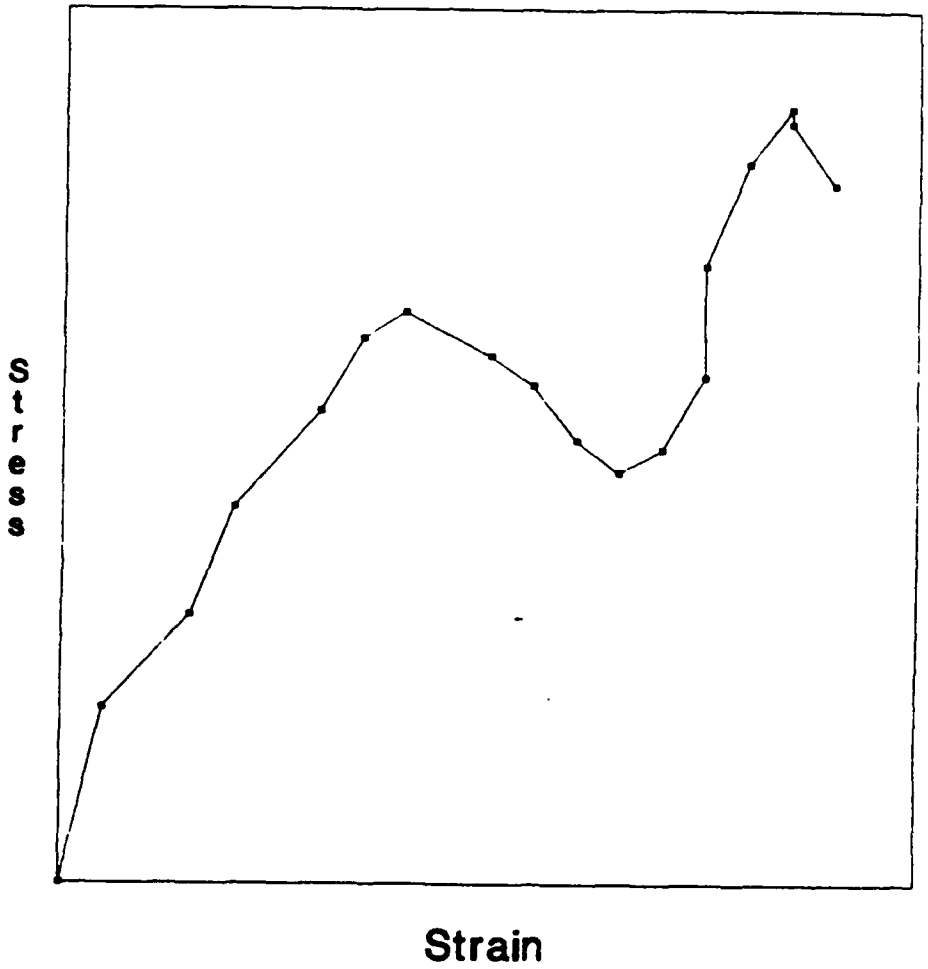

Figure 5.3 #1-68.95 kPa, Stress v. Strain.

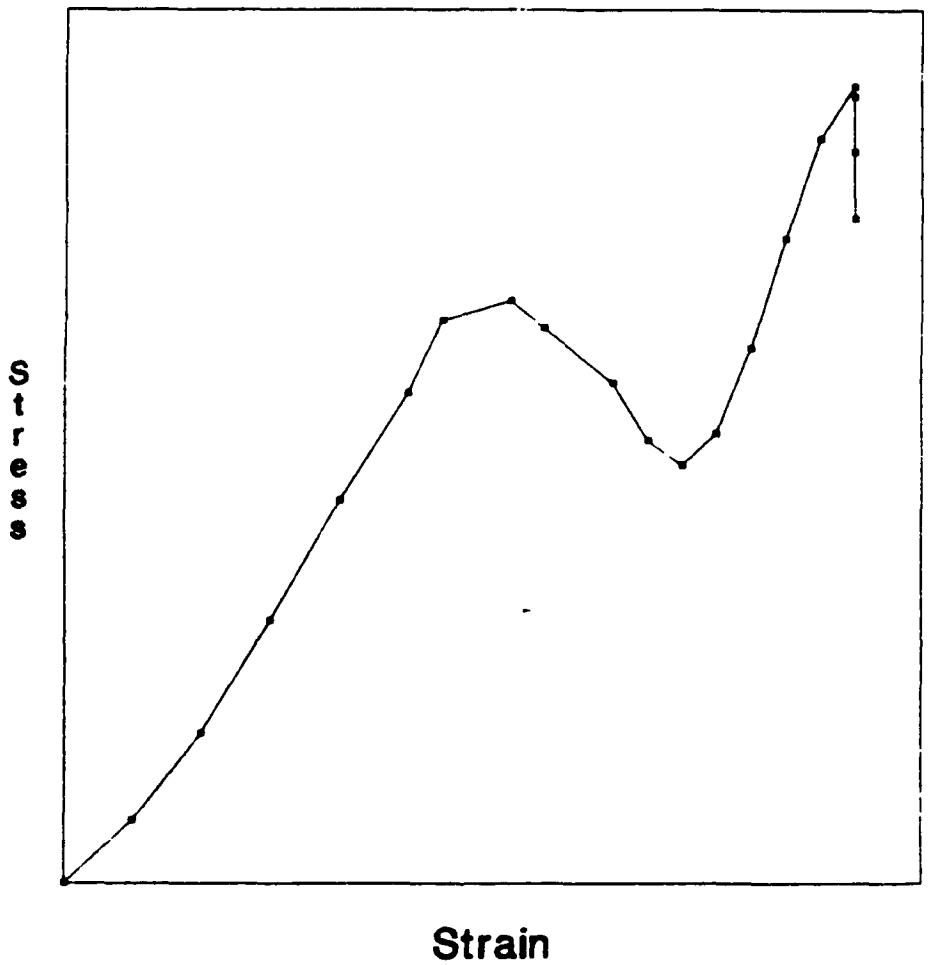

Figure 5.4 #5-137.9 kPa, Stress v. Strain.

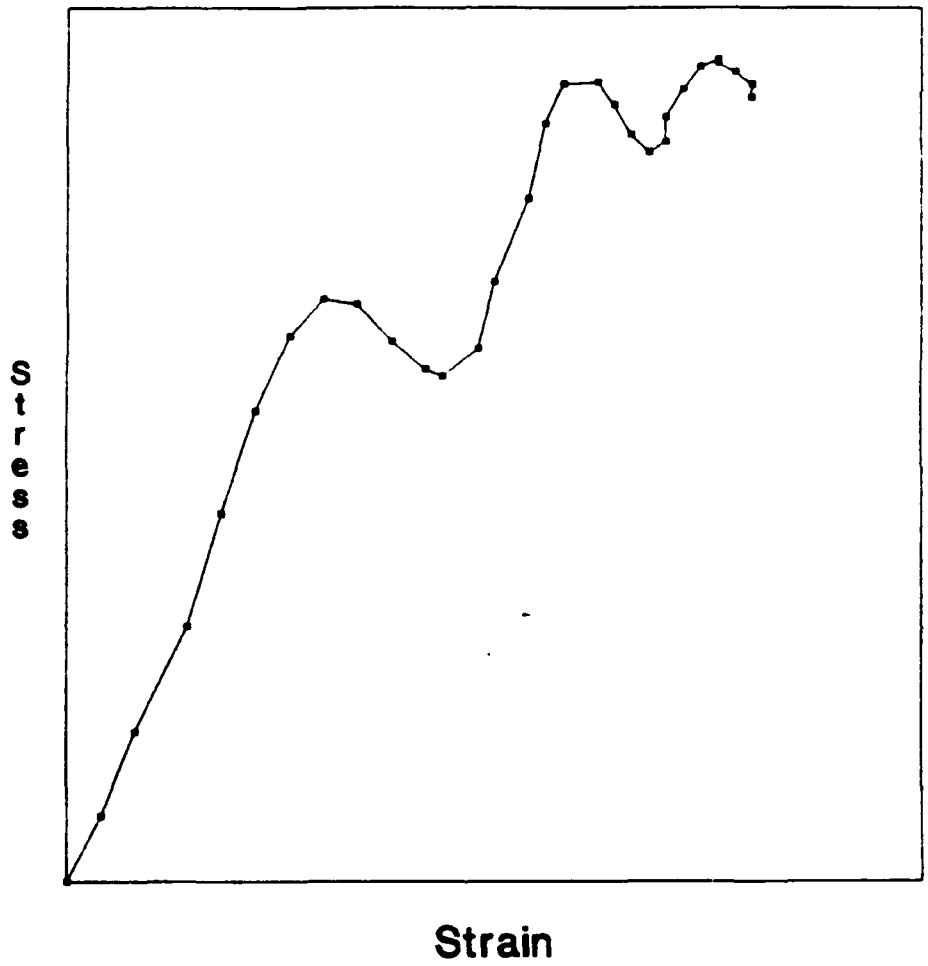

Figure 5.5 #3-206.85 kPa, Stress v. Strain.

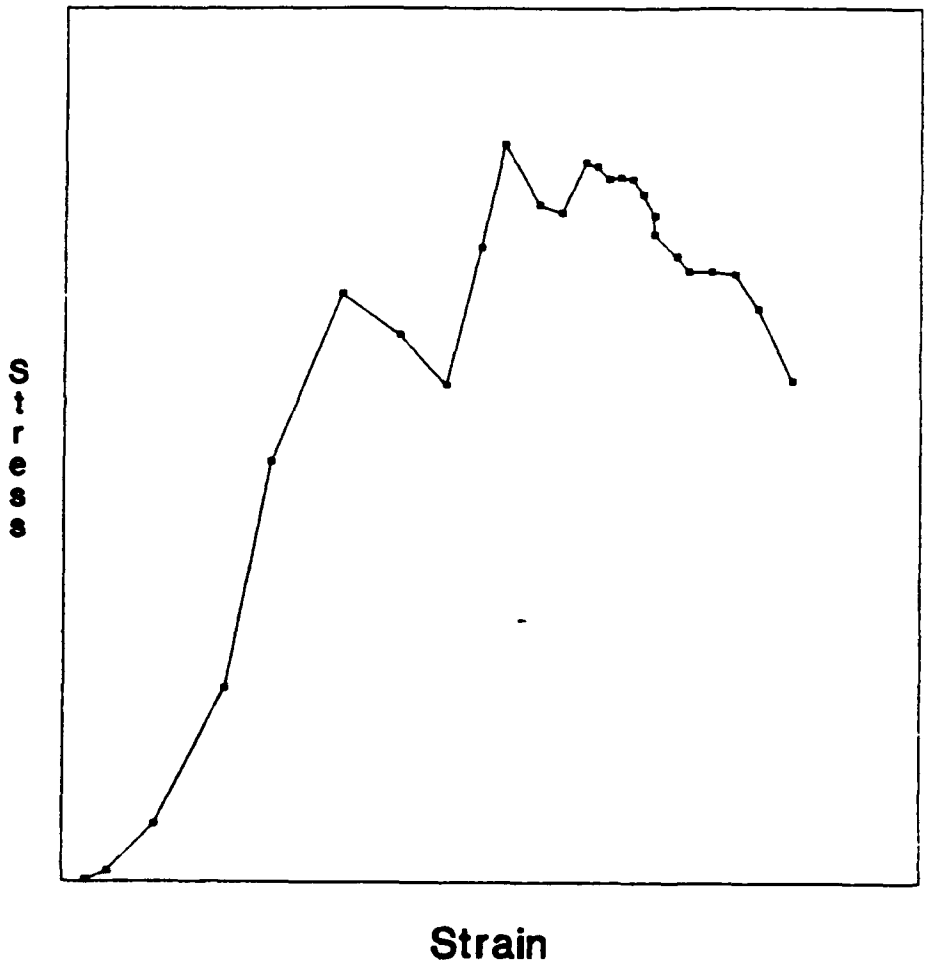

Figure 5.6 #2-275.8 kPa, Stress v. Strain.

fused to the stub face whenever the specimen fractured. Energy dispersive x-ray spectroscopy of the fused material showed it to contain iron and nickel from the stub and either aluminum and/or aluminum oxide from the specimen. It is presumed that during a test, aluminum from the material's matrix was melted through adiabatic heating caused by fragments shearing, and then deposited on the stubs. The existence of long, axially oriented fragments is further evidence that the specimens sheared. The frequency of refinishing decreased as the SHPB pressure and the resulting number of specimens that fractured decreased.

5.2 Microscopy Analysis

The material's microstructure was first examined by optical microscopy and, subsequently, by scanning electron microscopy (SEM). One whole, tested specimen from both 206.85 kPa and 275.8 kPa, and an untested specimen were longitudinally sectioned with a low speed diamond saw. The sections were then mounted in a conducting medium, ground, and polished. The grinding was done by hand on 240, 320, 400, and 600 grit papers, in order.

The sections were machine polished on a Buehler Ecomet® 3 variable speed grinder/polisher. The polishing regime for silicon carbide recommended by Buehler was

used. This procedure began with a 15 μ diamond slurry on Buehler's Metlap 10™ polishing disk. The specimens were polished for 3 minutes at 240 rpm under 11.34 kg load per sample, and were rotated counter to the direction of rotation of the polishing disk. The Metlap 4™ disk with a 6 μ diamond slurry was next used under the same load for 10 minutes at 120 rpm. The specimens were rotated in the same direction as the disk. The final stage consisted of a Texmet® cloth glued to a disk with a 1 μ diamond slurry. The specimens were polished for 30 minutes at the same speed and load, but again rotated opposite the rotation of the disk.

As seen in Figures 5.7 and 5.8, no differences in microstructure are seen to exist between the untested specimen and the tested specimen when observed through an optical microscope. There are, however, four, distinct phases visible. Energy dispersive x-ray analysis, with the beryllium window removed to detect light elements, was used to identify the phases. Figure 5.9 shows the phases and their identities. Figures 5.10, 5.11, and 5.12 are the spectra obtained for the phases identified as aluminum, aluminum oxide, and copper-aluminum, respectively. The light gray phase, containing aluminum and copper, is a copper aluminum compound; $CuAl_2$. The copper is a dopant used in the oxidation process. The

Figure 5.7 Untested Specimen Microstructure (x40). Al/Al_2O_3 matrix shown with SiC Particles.

Figure 5.8 206.85 kPa Specimen Microstructure (x40). No change in microstructure after testing.

Figure 5.9 Identification of Microstructure Phases (x40). Region #1--Aluminum, Region #2--Alumina Region #3--Copper-Aluminum.

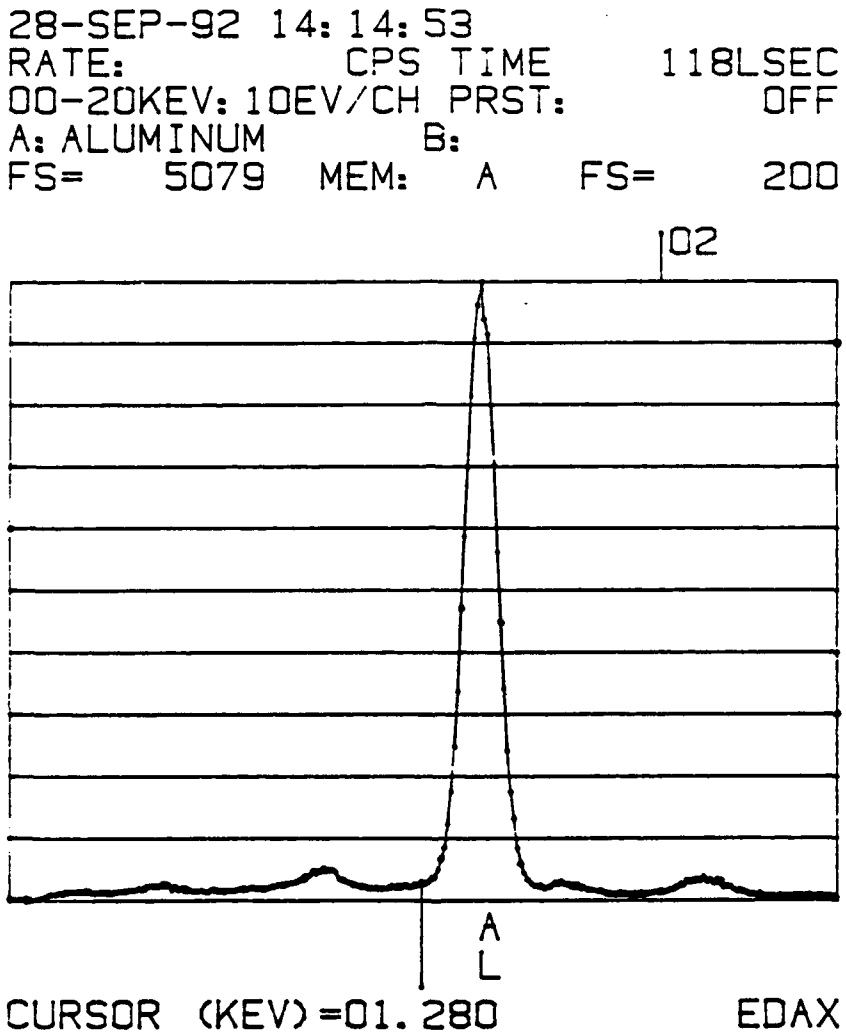

Figure 5.10 Aluminum Phase Spectrum.

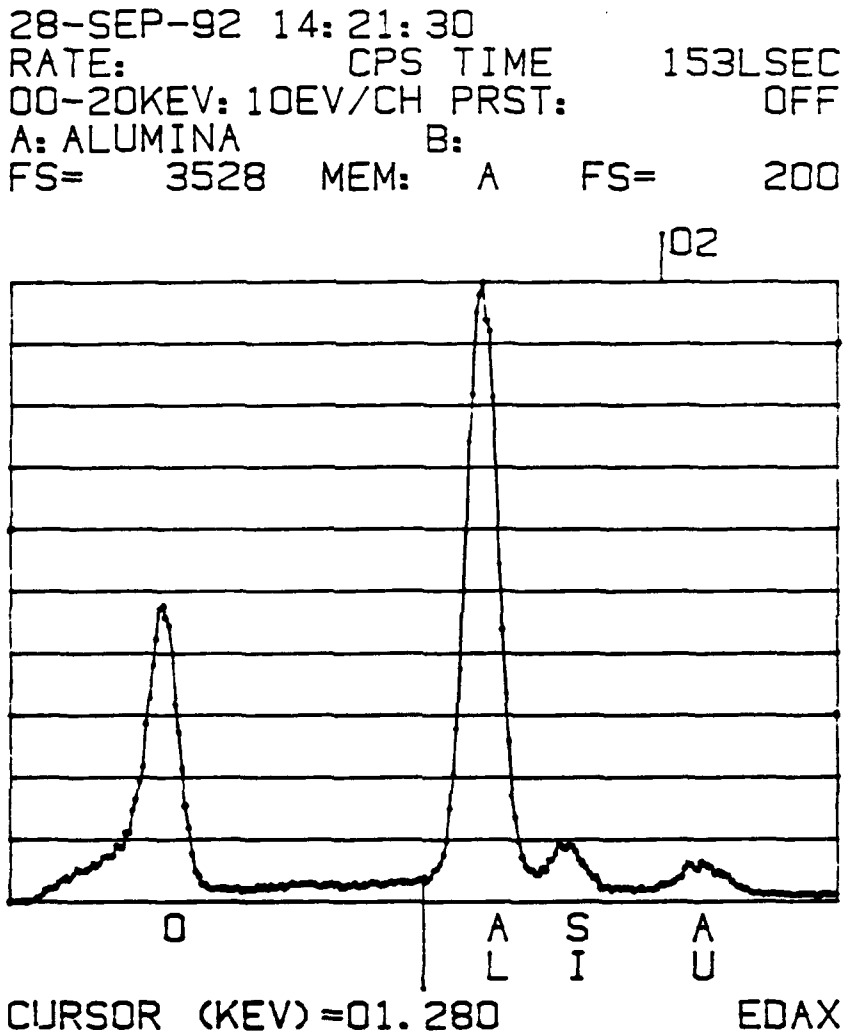

Figure 5.11 Aluminum Oxide Phase Spectrum.

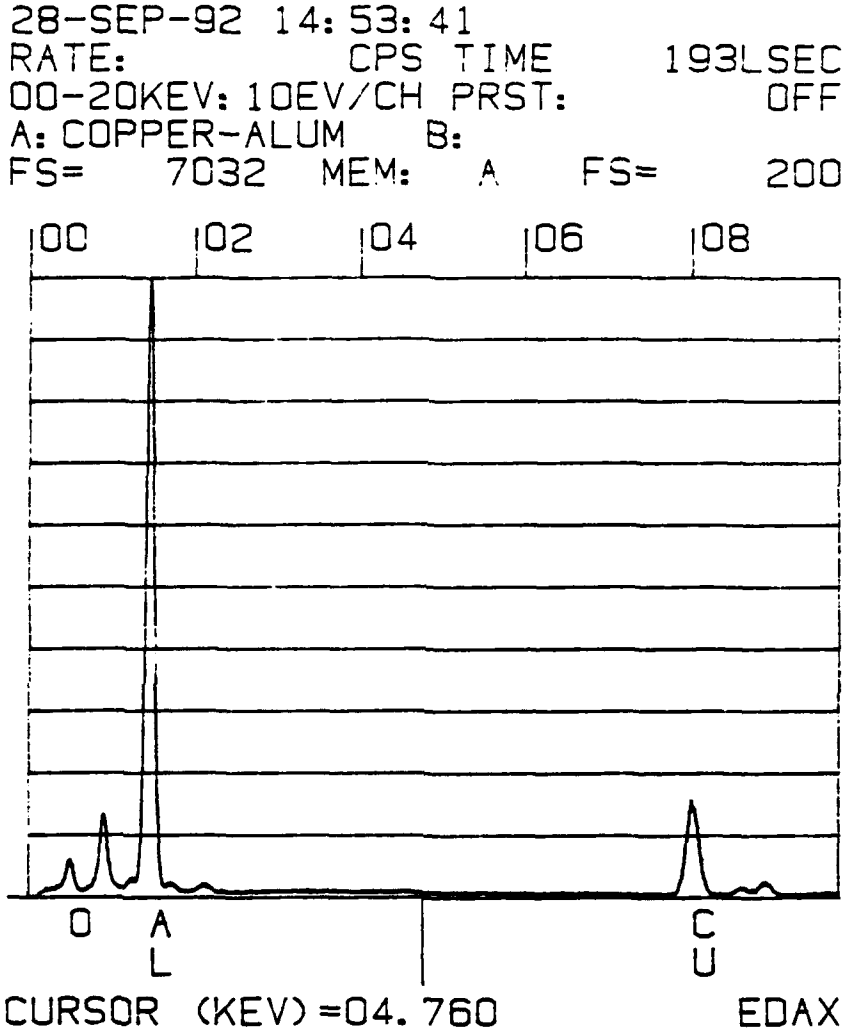

Figure 5.12 Copper-Aluminum Phase Spectrum.

presence of zinc was also detected.

Numerous pores were also observed in the silicon carbide particles but not in the ceramic matrix (Figure 5.13). This indicates that the melt oxidation process resulted in a completely interconnected, non-porous matrix. The matrix strength should thus be the highest possible given the processing conditions and controls, and the concentrations of the elements.

Selected fractured SHPB specimens were also examined by SEM. The selected specimens were mounted on aluminum stubs with silver conducting paint. The mounted specimens were sputtered with gold to make them electrically conductive.

Electron microscopy revealed the existence of crack branching and crack deflection (Figure 5.14) as two of the material's fracture toughening mechanisms. The cracks seen in Figure 5.14 were observed on the exterior of a fractured specimen. The porosity observed from optical microscopy of the microstructure was again observed in the fractured specimens. Figures 5.15 and 5.16 show pores in specimen #3 at 68.95 kPa and specimen #2 at 206.85 kPa, respectively.

Several differences were noted between the specimens that fractured at 206.85 and 275.8 kPa, and the specimens that fractured at 68.95 and 137.9 kPa. As seen

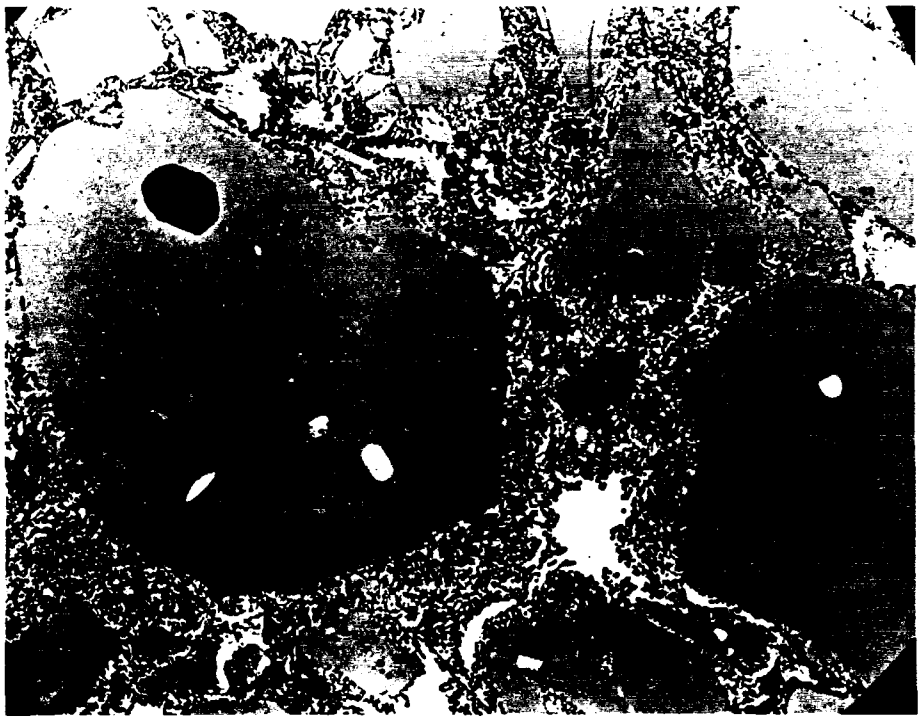

Figure 5.13 Pores in SiC Particles (x20).

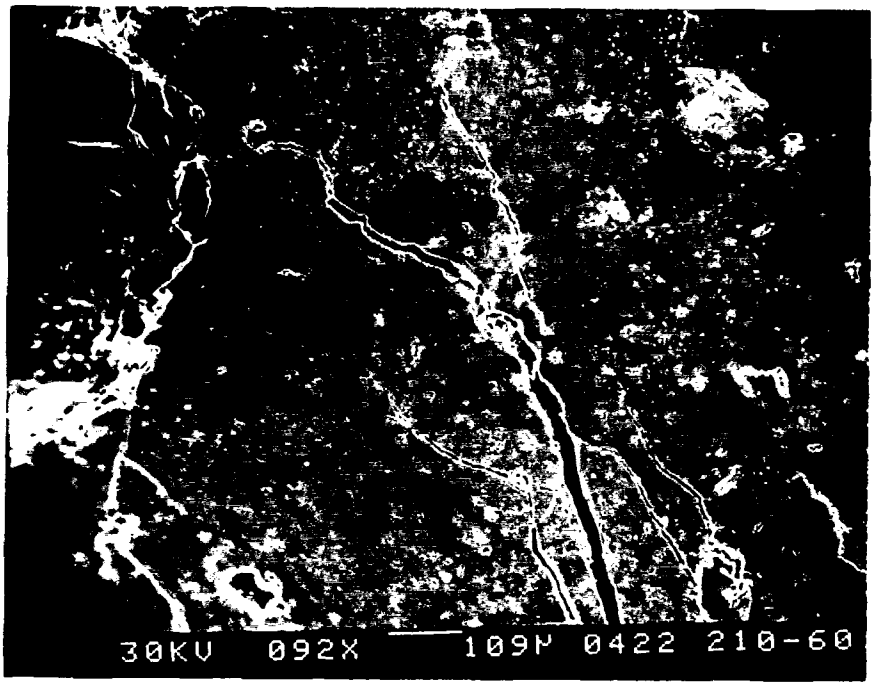

Figure 5.14 Crack Branching and Deflection.

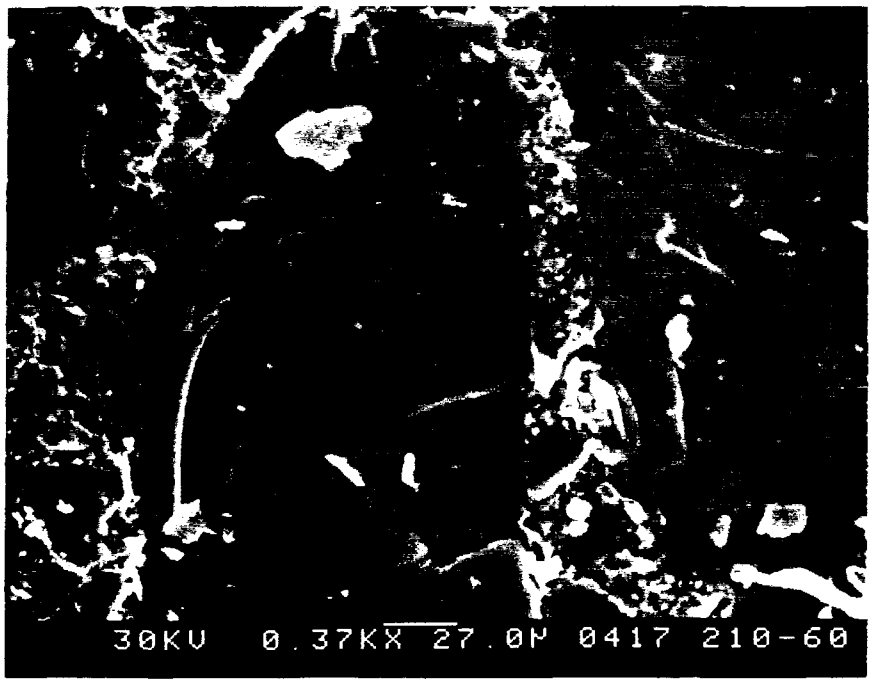

Figure 5.15 Pore in 68.95 kPa Specimen.

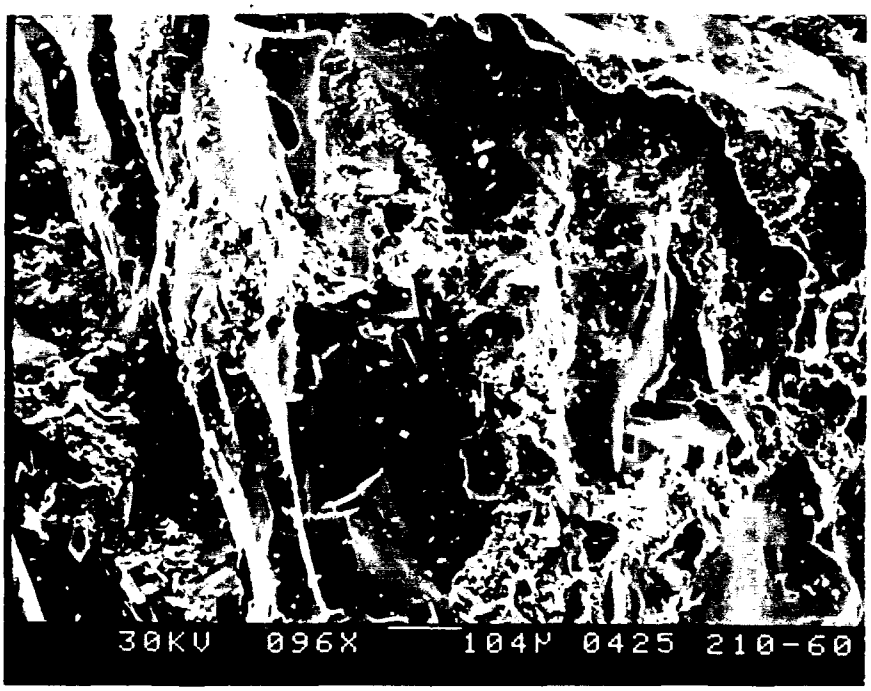

Figure 5.16 Pores in 206.85 kPa Specimen.

in Figure 5.17, the higher kPa fragments showed extensive microcracking parallel to the compressive axis in the silicon carbide particles. (The arrows in the micrographs indicate the direction of the compressive axis.) It was also observed, in Figure 5.18, that the material's pores became sites of microcrack nucleation and growth.

Microcracking was not observed in any of the specimens that fractured at 68.95 and 137.9 kPa. The transgranular fracture of the silicon carbide particles is shown in Figure 5.19. A textured border can also be seen surrounding the particles. Energy dispersive x-ray analysis of the textured boundary indicated that this region contained aluminum. It is presumed that the textured border is the aluminum oxide/aluminum matrix. No evidence of fracture along the interface between the matrix and the particles was observed and indicates the existence of strong interfacial bonding.

At the lower strain rates, the induced stresses caused the growth of microcracks which coalesced into larger cracks which, in turn, caused the specimens to fragment. No evidence of any residual microcracks remained presumably because all of the energy from the test was absorbed in the fragmentation process. At the higher strain rates where residual microcracks were observed in the silicon carbide particles, a portion of

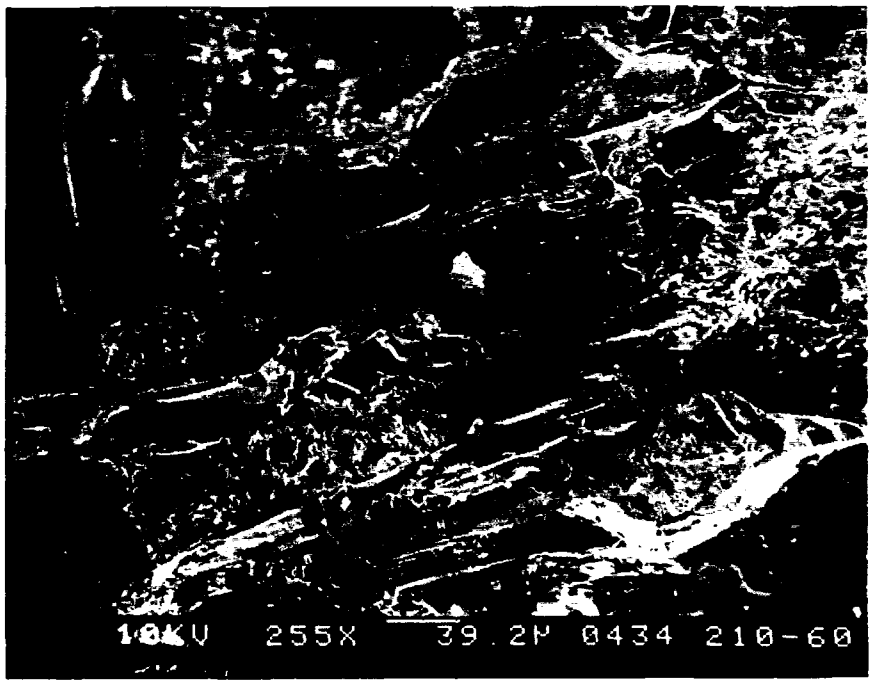

Figure 5.17 Microcracking in SiC Particle.

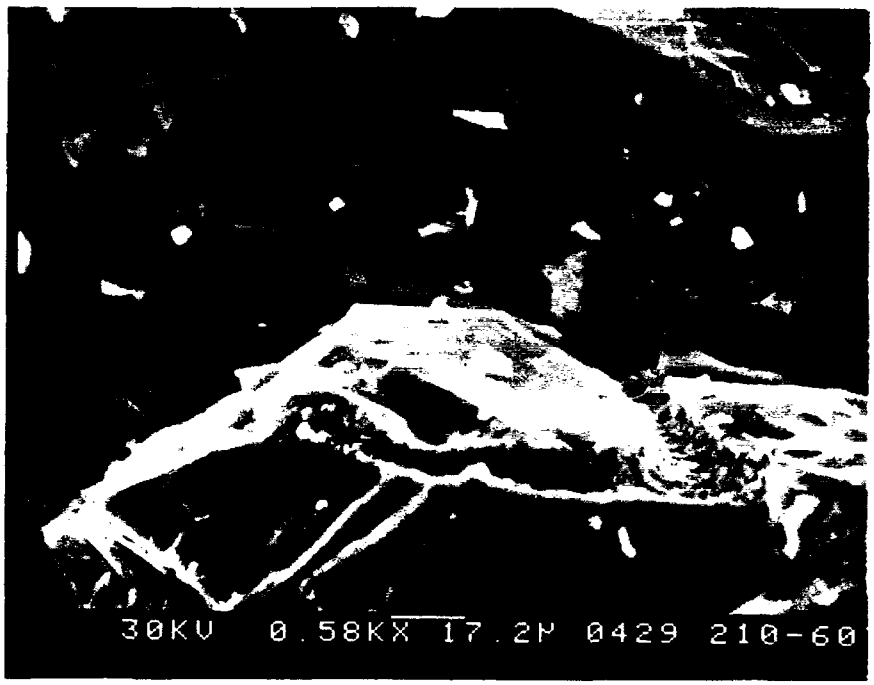

Figure 5.18 Microcrack from Pore.

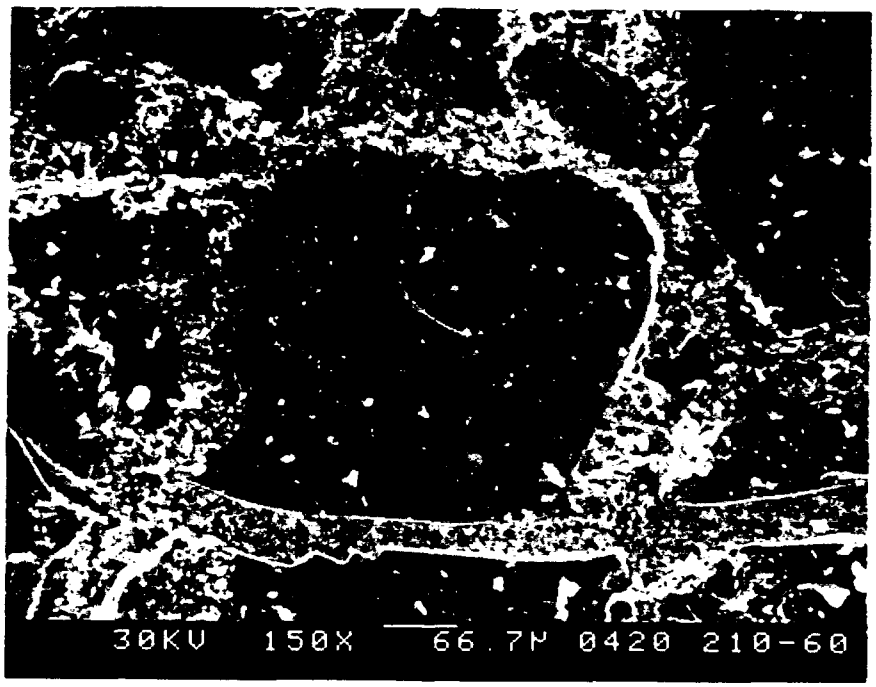

Figure 5.19 Fracture of SiC Particle.

each test's energy went into the fragmentation process (which was more extensive) and the excess was absorbed by the material in the formation of the residual microcracks. It also seems apparent that the suppression of microcrack growth by the material's inertia, as described by Lankford [4], is seen in the higher strain rate specimens.

It is not totally clear why, given the same outer chamber pressure, some specimens fragmented and others did not. It was proposed earlier that nonparallel specimens contributed to premature fracture. However, given the existence of the pores in the silicon carbide particles and the microcracks that were nucleated from the pores at the highest strain rates, it is possible to conclude that in the lower strain rates, the porosity of the particles in the fractured specimens may have been greater than in the unfractured specimens and thus have lowered the fractured specimens' fracture toughnesses. For the higher strain rate specimens, where the increased striker bar velocity acted as a catalyst, a combination of the particles' porosity and the development of microcracks from the pores resulted in the greater number of fractured specimens. The single 275.8 kPa specimen that did not fracture may have had a lower porosity than the other 275.8 kPa specimens.

Lankford, in studying the compressive fracture of a commercial alumina with a glassy phase, concluded that pores in the alumina were important in the granulation process that was observed [6]. The pores were seen to act as microcrack initiation sites and/or channels for propagating microcracks.

Thus, the particles appear to affect the compressive strength of the material. The role played by the particles is in contrast to the earlier mentioned results from a whisker reinforced ceramic composite [7]. The conclusion from that work was that the composite's high strain-rate behavior was not influenced by the presence of the whiskers.

A very limited transmission electron microscopy (TEM) was performed in order to improve the understanding of the material's microstructure [25]. Discs, 3 mm in diameter, were core drilled from slices of untested and tested specimens. The discs were mechanically thinned to ~200 μm and then dimpled on a Gatan Dimpler to a thickness of ~20 μm. The discs were then ion milled on a Gatan DuoMill at 4 keV and a beam angle of 12° until perforation.

Examination of the specimens in a Philips EM 400T TEM at 120 keV revealed that, in the untested specimens, the silicon carbide particles consisted of large, single

crystals while the aluminum oxide matrix had a much smaller grain size, typically 1-2 μm in diameter. The interfaces between the aluminum oxide and silicon carbide grains were observed to be clean and featureless with no evidence of any interfacial reaction product. Figure 5.20 shows aluminum oxide grains containing many small pores and inclusions. Energy dispersive x-ray analysis of the inclusions showed them to be rich in elements such as copper, zinc, and chromium. No attempt was made to make any quantitative analyses.

The small percentage of aluminum in the matrix was present as discrete single crystal areas that were typically 0.5 μm in width and .02 μm in length. The aluminum grains contained a few dislocations, presumably generated during cooling from the fabrication temperature as a result of the stresses induced by the difference in the coefficients of thermal expansion between the ceramic phases and the aluminum (Figure 5.21). These small, crystal areas represent sections through small portions of the original molten metal channels which enabled the directional oxidation phenomenon to proceed.

Although the ceramic phases showed some evidence of the shock loading, the most notable difference after testing concerned the aluminum which had clearly undergone extensive plastic deformation. The plastic deformation

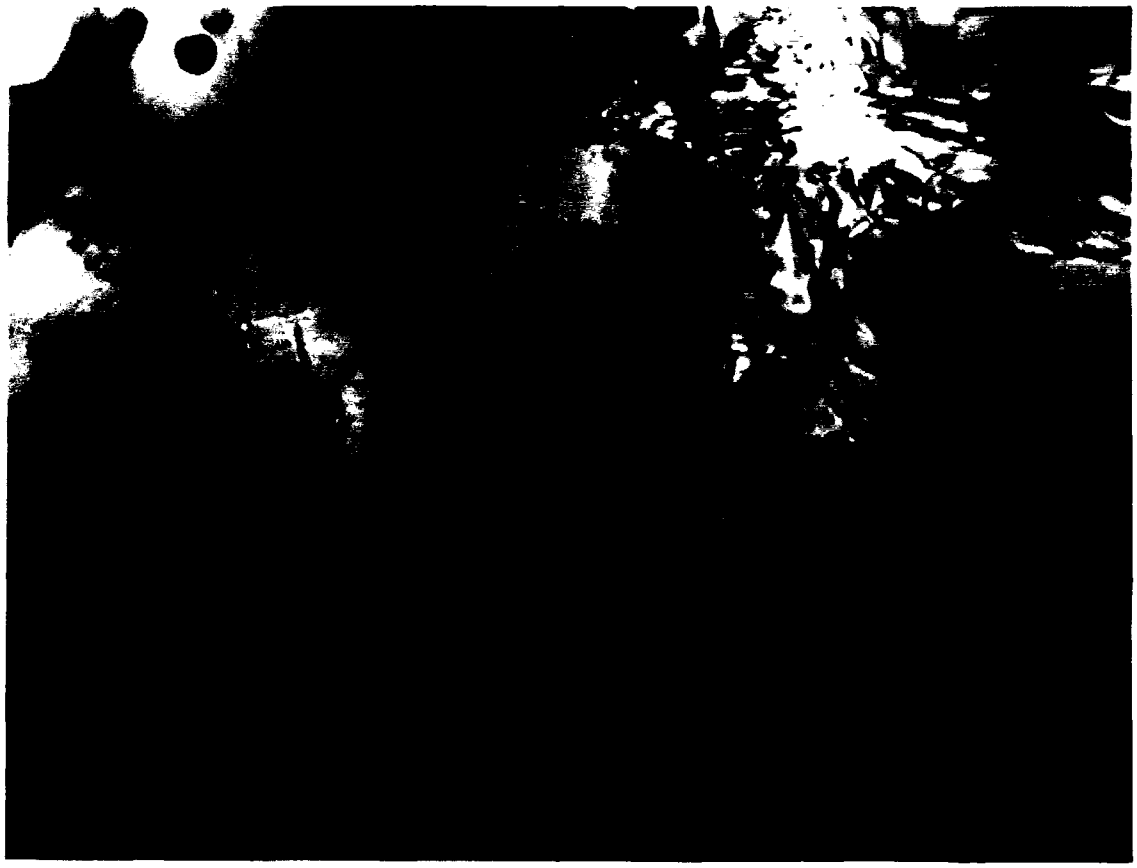

Figure 5.20 Aluminum Oxide Grains (x70,000).

Figure 5.21 Random Dislocation Distribution in Al Grain Before Testing (x70,000).

had two components. First, the previously single crystal grains had undergone such severe deformation that subgrain formation and/or dynamic recrystallization had occurred, giving rise to ~0.1-0.2 μm sized new grains (Figure 5.22). Second, there were many locations where the aluminum had been extruded into cracks which had formed in the ceramic phases (Figure 5.23). In these regions, the fragments of the ceramic phase were effectively held in place by the aluminum.

The silicon carbide also occasionally showed evidence of plastic deformation as shown in Figure 5.24, where the dislocations can be seen emerging from a crack.

5.3 Low Strain-rate Results

Six SHPB specimens were compression tested on an Instron servo-hydraulic test machine. Three specimens each were tested at strain rates of 3.509 /sec. and .351 /sec. The results of the testing are shown in Table 5.5. The highest compressive ultimate strength 819.41 MPa was ~4 MPa greater than the lowest SHPB ultimate strength. Figure 5.25 shows a low strain-rate typical stress v. strain curve.

It was also noted that the specimens fractured into the same long, axially-oriented flakes that were

Figure 5.22 Recrystallization in Aluminum Grain as a Result of Testing (x90,000).

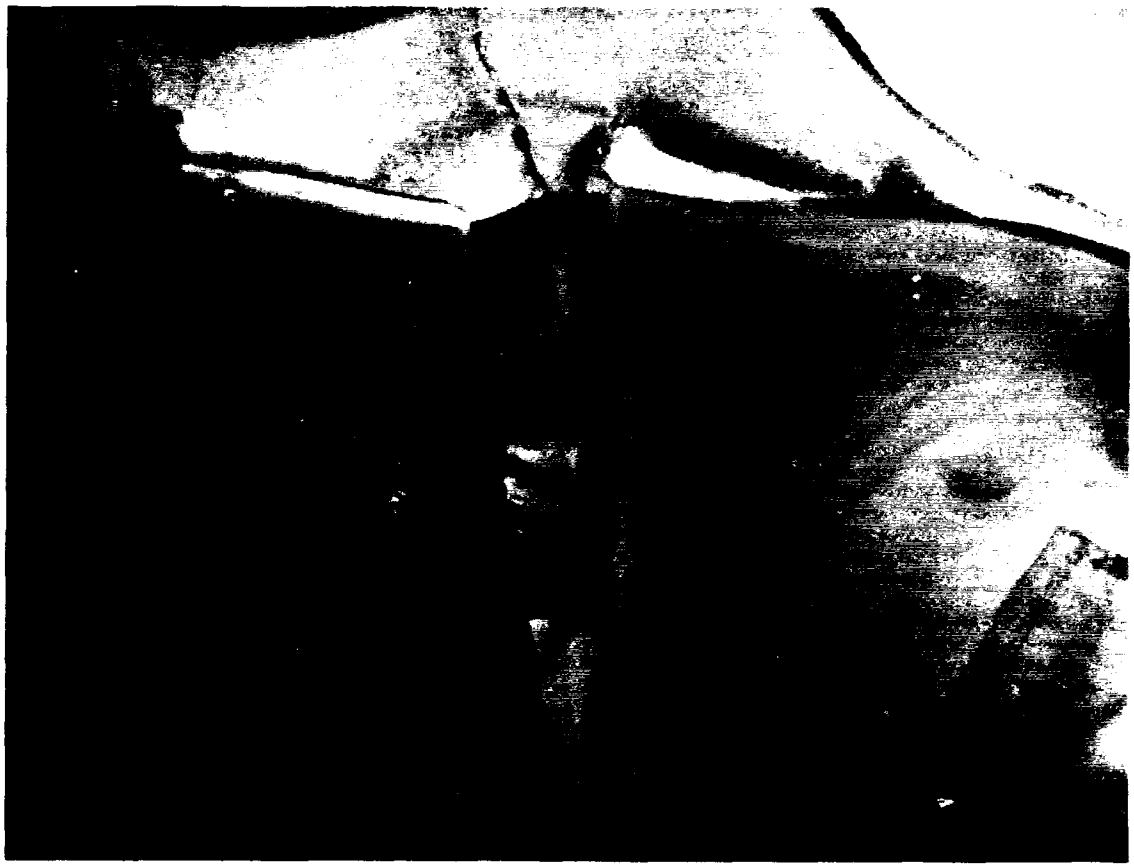

Figure 5.23 Aluminum Extruded into Crack (x140,000).

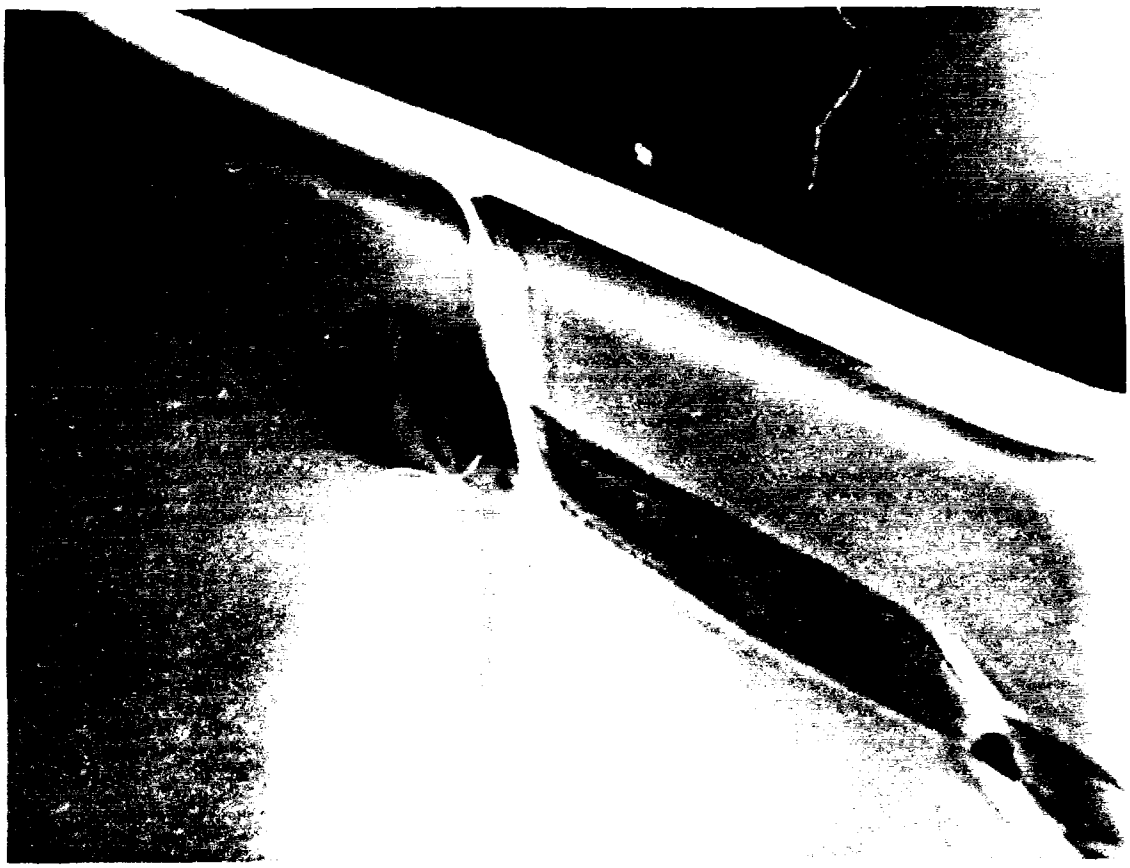

Figure 5.24 Plastic Deformation in SiC Particle (x90,000).

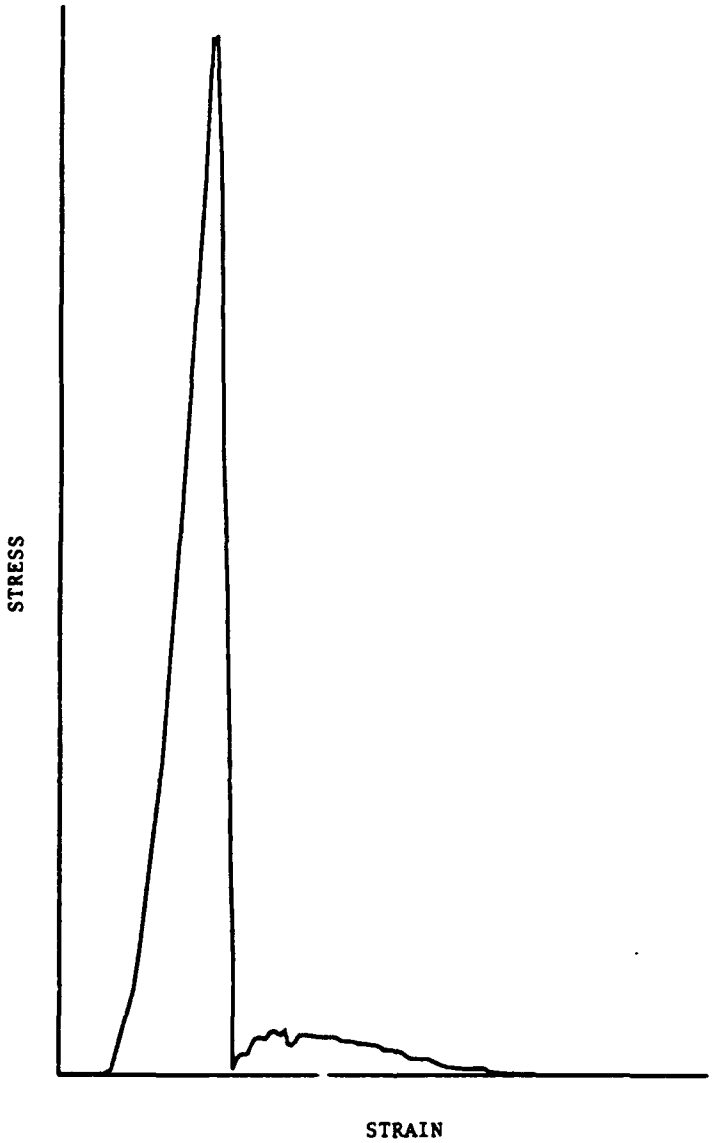

Figure 5.25 Low Strain-rate Stress v. Strain Curve.

observed in the high strain-rate testing, although the number of fragments, in general, appeared to be less.

Table 5.5 Low Strain-rate Results (MPa).

Strain Rate (/sec.)	Specimen #		
	1	2	3
3.509	112.15	128.18	125.43
.351	787.37	819.41	650.04

Analyzing the results shown in Table 5.5, it is unclear why, contrary to expectations, the compressive strengths at the lower strain rate were higher than the strengths at the higher strain rate. This result may not be caused by any specific material behavior but may be due to the operation of the test machine; since the hydraulic machine which was used cannot immediately exert the higher strain rate at the beginning of the test. There is then a ramping effct, the characterizations of which are well known. Also, the higher strain-rate specimens were tested first when the hydraulic system in the machine may not have been fully exercised and warmed up. The testing at the lower strain rate may have coincided with the test machine reaching its full operating potential.

In summary, all of the results for the mean ultimate stress v. mean ultimate strain rate are presented

in Figure 5.22. This figure shows the gradual strain hardening of the material from low through high strain rates.

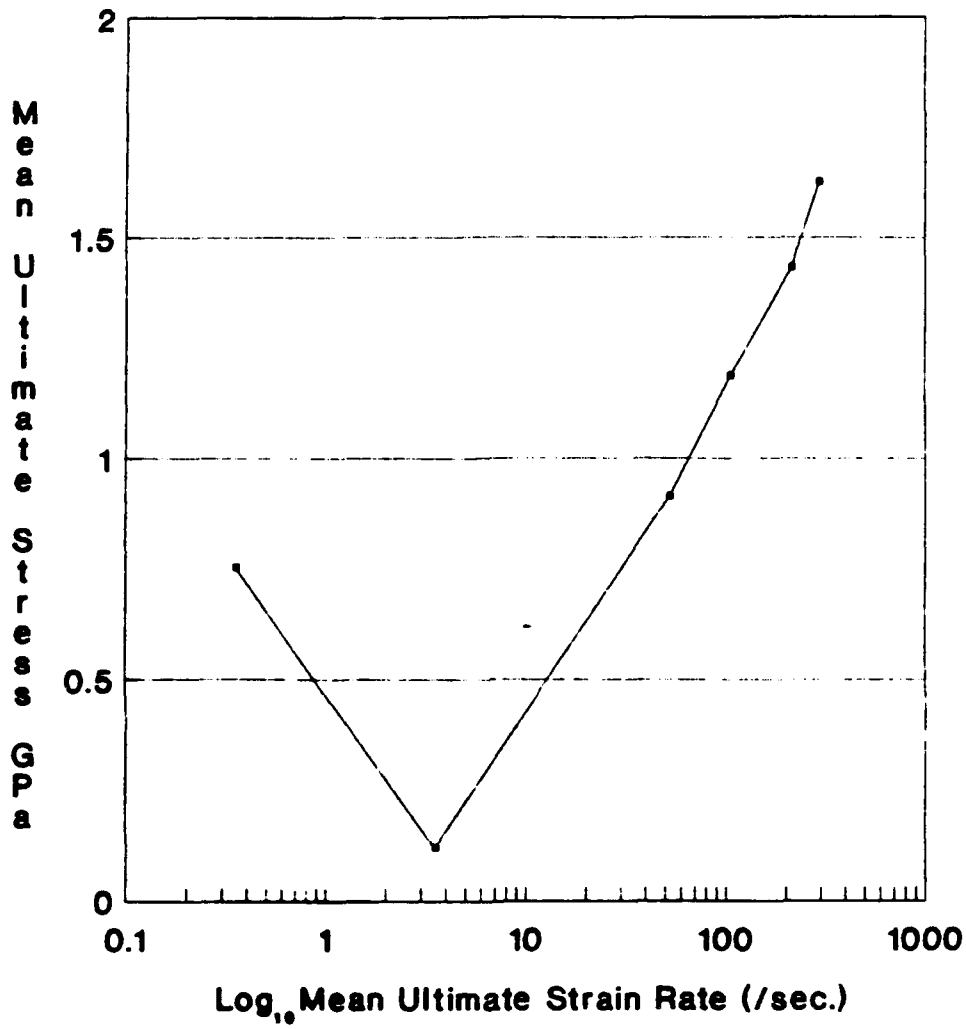

Figure 5.26 Mean Ultimate Stresses v. Mean Ultimate Strain Rates.

Chapter 6

CONCLUSION

6.1 Conclusions

A particle reinforced ceramic matrix composite, manufactured by the Lanxide® DIMOX™ process, was compression tested at high strain rates in the Split-Hopkinson Pressure Bar. Additional low strain-rate testing was done to characterize more fully the material's strain rate response.

Values for the material's ultimate compressive stresses, strains, and strain rates were calculated and analyzed. It was shown that, as the SHPB outer chamber pressure increased, the associated mean ultimate strain rates increased from 52.38 /sec. to 291.27 /sec. With each increase in the mean ultimate strain rate, the material's mean ultimate stress and strain increased. This reflects a degree of strain-rate sensitivity in the material.

Optical microscopy of tested and untested whole specimens revealed no apparent microstructural change in the material as a result of testing. This response leads to the conclusion that the tested, whole specimens absorbed the energy of each test in the form of elastic strain energy. Thus the aluminum and copper-aluminum phases in the matrix enabled the material to elastically absorb and release the strain energy of the test. Optical microscopy also revealed the existence of pores in the silicon carbide particles.

Electron microscopy of the fractured surfaces revealed a change in the material's behavior at the higher strain rates. Residual microcracks were observed in the fractured specimens tested at 206.85 and 275.9 kPa. The pores in the silicon carbide particles also became sites for microcrack nucleation and growth. No microcracking was observed in the fractured specimens tested at the lower SHPB pressures.

Plastic deformation of the aluminum in fractured specimens was shown in the limited TEM microscopy. The deformation caused subgrain formation and/or recrystallization of the aluminum grains and extrusion into cracks in the aluminum oxide matrix and silicon carbide particles.

The test results from the low strain-rate testing are not considered very reliable or representative of the material's actual response. Further testing is necessary in the area in order to confirm the effects noted here.

It appears then that when the material fractures at the higher strain rates, it dissipates the energy of the compressive pulse via plastic deformation of the aluminum and extensive microcracking in the silicon particles parallel to the compressive axis. Shearing, evidenced by the adiabatically heated aluminum that was fused to the faces of the removable stubs, is also present and increases the amount of energy dissipated. Any remaining energy is absorbed by the silicon carbide particles in the form of residual microcracks. At the lower strain rates, the induced stresses caused the growth and coalescence of microcracks into larger cracks which, in turn, caused the material to fragment into fewer, larger pieces.

The role of the silicon carbide particles is to provide the majority of the material's compressive strength while the aluminum, which can be thought of as imbedded in a three dimensional aluminum oxide mesh, increases the fracture toughness. The effect of the aluminum oxide mesh is to strengthen the aluminum and lessen its plastic deformation.

The wide scatter in the SHPB data is mostly attributed to two causes. The first cause is the sensitivity of the ultimate strain rate to the time at which the ultimate point is chosen. As shown earlier, the minimum point on the transmitted wave varied widely in time, and thus caused the corresponding strain rates to vary. The second cause was the difficulty in manufacturing consistently true specimens. It is likely that the tested specimens that remained whole were truer than the specimens that fragmented.

6.2 Suggestions for Further Research

Continued SHPB testing of the material using more precise specimens at strain rates $\geq 10^3$ /sec should be performed next. This testing, coupled with some quasi-static testing, will provide a full characterization of the material's response to varying dynamic compressive loading conditions. Acquiring a better picture of the role played by the aluminum in the matrix can be accomplished by testing the same material but with differing volume fractions of aluminum. Knowledge gained from this testing can be utilized in better tailoring of the material's composition to fit the intended use. Finally, SHPB tests of the Lanxide® unreinforced Al_2O_3/Al composite would provide an indication of the importance of the SiC particles in the tested composite.

Appendix A

SPLIT-HOPKINSON PRESSURE BAR OPERATING MANUAL

SPLIT-HOPKINSON PRESSURE BAR OPERATING MANUAL

005 SPENCER LAB
Mechanical Engineering Department
University of Delaware

by

D. S. Pritchard

H. S. Yoon

Revised

by

T. J. Frey
September 1989

and

J. M. Parker
October 1992

STANDARD OPERATING PROCEDURE FOR THE UNIVERSITY OF DELAWARE SPLIT-HOPKINSON PRESSURE BAR

I. The Apparatus and Instrumentation

One of the most widely used experimental configurations for high strain-rate material properties testing is the Split-Hopkinson Pressure Bar. The apparatus at the University of Delaware is shown in Figure 1. It consists of a striker bar and two pressure bars mounted and aligned on a rigid base. The striker bar is accelerated for impact by using the energy stored in a gas gun. At the impact, an elastic compressive wave is generated and travels down the first bar (no. 1) at the elastic wave velocity. The specimen positioned between the two pressure bars, is deformed by stress waves. An elastic wave is then transferred through the second pressure bar (No. 2). The inferred dynamic stresses and strains in the specimen are determined by the strain gauges attached on each pressure bar equidistant from the specimen. The two pressure bars are each instrumented with full strain gauge bridges for better sensitivity and the canceling of the slight bending effects present in the long bars. Radial deformation in the bars is also canceled. The velocity of the striker bar is measured by using two infrared light beams at a set distance (4 in.) apart. This distance is d. When the first beam is broken a timer is started. Breaking of the second beam turns the timer off. This yields Δt. The velocity of the striker bar (V) is thus:

$$V = \frac{distance}{time} = \frac{4\,inches}{\Delta t}$$

The magnitude of the striker bar velocity is controlled by the force of the gas from the outer pressure chamber expanding in the gun barrel. Extreme care must be taken when firing the striker bar or severe injury to the operator may result.

II. Switching On and Adjusting Instrumentation

The oscilloscope is equipped with high gain preamplifiers very sensitive to the slight noise that can be generated in the electronic system. Therefore, sufficient warming up (about 30 minutes) of the instrument (especially the preamplifiers) is needed to get accurate gauge signal voltage readings.

1. Switch on the strain-gauge preamplifier, striker bar velocity timer, and the oscilloscope.

NOTE: Disk drive switch should be ON at all times. Power will be controlled by oscilloscope switch.

2. Set up the preamplifier.

a. Initially set the desired excitation on each channel with the channel selector knob of the preamplifier. The excitation should be 10 volts. Adjust the BRIDGE EXCIT by using a small screwdriver to read the desired voltage with EXIT and CAL switches in the OFF position.

NOTE: Channel 1 is for the Bar 1 front strain gauge (trigger). Channel 2 is not currently used. Channel 3 is for the Bar 1 rear strain gauge. Channel 4 is for the Bar 2 strain gauge.

b. Initially adjust each AMP BAL with a small screwdriver until both output lamps are off.

c. Initially adjust GAIN for each channel (recommend 200 on a scale of 0 to 1000 on the GAIN potentiometer).

d. Turn EXCIT switch to ON and adjust BALANCE control to extinguish OUTPUT lamps and turn lock knob to lock in place.

NOTE: If right output lamp is lit, turn balance knob clockwise until lamp goes off. If lamp goes off only when balance knob is turned all the way, gauge may not work properly on next test. Conducting a practice test (without a specimen) may return it to the proper balance. There may also be vibration in the bars caused by the Machine Shop above or the ventilation machinery housed next door.

NOTE: Step a-c should not need to be readjusted once initially set.

3. Check the velocity timer by pressing the **TEST** button. The numeric value should be 2048 in a normal condition.

NOTE: If timer reads 2049 or 3075, conducting a practice test or re-pressing the test button several times will return it to read 2048. If the velocity timer

reads "...." or "2.0.4.8" press reset button and test button again.

4. Adjust the trigger level of the oscilloscope (Reference to the Nicolet manual 8-30 to 8-42).

5. Adjust the oscilloscope settings as desired. It is recommended to set the scope as follows: (Reference Nicolet manual)

a. Time per point - 1 μs

b. ± Volts full scale - 20 V

c. Memory - ALL

d. Auto/Norm - NORM

e. Slope - DUAL

f. Source - EXT (Bar No.1 signal should be fed into Channel A. Bar No. 2 signal into Channel B, and the trigger signal into the External Channel.

g. AC/DC/GND - AC (where plugged in), GND (where not plugged in)

h. Avg., Pt. Avg., Filter, Save Ref, View - switches in DOWN position.

i. X/Y or Y/T - Y/T

j. Vertical and Horizontal Expansion - OFF

k. Function - RESET NUM

l. Autocenter/Zero - OFF

m. AC/DC - AC

6. Check the triggering signal for the oscilloscope by tapping the No. 1 bar by hand into the No. 2 bar. Before checking the signal, the storage control mode should be in the <u>LIVE</u> and <u>HOLD NEXT</u> position (lamps lit).

7. Insert blank floppy disk into left side disk drive. Insert pointer into hole above "auto-center". The word "For" should appear on the disk drive display. Push the "store" button to format the disk. It takes

approximately 5 minutes to completely format the disk for 20 tracks. The above only needs to be performed once for each disk. Push "up" or "down" until the proper track number is displayed. **NOTE:** It is suggested to record waves on odd track numbers and the corresponding integrated wave (see Analysis) on the next, even track.

III. Mounting the Tensile Specimen

NOTE: Dimensions of specimen must be recorded prior to test.

a. Put the striker bar in the firing position by using the stiff wire provided. The striker has to be moved toward the pressure chambers until it stops.

b. Pull out the No. 2 bar from the dashpot and reposition it with the UP marking showing correctly.

c. Reposition the No. 1 bar to match the marker on the specimen end of the bar with the nearest Teflon bearing block supporting the No. 1 bar and with the UP marking correctly showing.

d. Put the sleeve on either bar and push it out of the way for the next step (refer to Figure 2).

e. Insert the specimen into the bars. Specimens should be screwed into both bars simultaneously. All threads of the specimen are to be just engaged with the bars. Be careful of leads to gauges during this step.

f. Place the split collar over the specimen and tighten the split collar by twisting the bar slightly while applying pressure to bars No. 1 and 2 by hand.

g. Move the sleeve over the split collar.

h. Re-check the No. 1 bar position marker.

IV. Mounting the Compression Specimen

NOTE: Dimensions of specimen must be recorded prior to test.

a. Repeat step A, Part III.

b. Screw compression plugs into the bars tightly. Tightness of the compression plugs must be checked before each firing (see Figure 3).

c. Lubricate flat ends of bar and specimen with moly' denum disulfide powder.

d. Center the specimen as in Figure 3.

e. Applying sliding pressure to bar No. 2 until marker on bar is aligned as in Step C, Part III.

f. Position specimen catcher.

V. Rechecking the Electronics Just Prior to Firing

a. Check the balance of the gauge preamplifiers (lamps should be off).

b. Press the test button of the velocity indicator (2048 should be read).

c. Press the reset button of the velocity indicator.

d. Make sure the oscilloscope is ready. The storage control buttons on both side should indicate LIVE and HOLD NEXT until firing.

e. Recheck the balance of the gauge preamplifiers by glancing at the indicator lights just prior to firing. The gun operator is the only one to do this. All other persons must be in the control room at this stage. Gun operator may reposition balance and check scope to make sure it has not triggered.

VI. Pressurizing the Chambers (Reference Figure 1)

a. Make sure all valves are closed except the trigger valve (v7). It must be open (turned full-up - see Figure 1). All pressure gauges should read zero pressure.

b. Open the main valve (v1) of the high pressure tank (upper line) and control the regulator valve (v2) to indicate 200 psi (G1). **NOTE:** Replace nitrogen tanks if tank pressure falls below 100 psi.

c. Control the regulator valve (v5) of the low pressure line (lower line) as above.

d. Close the triggering valve (v7) by turning it full down (vertical). The triggering valve should always be open (full up horizontal position) when the gun is not in use.

e. Pressurize the inner chamber and the outer chamber step by step. (Pressure difference shouldn't exceed 20 psi).

1. First, by opening the inner line valve (v6) pressurize the inner chamber up to 20 psi (G5), and then by opening the outer line valve (v3) pressurize the outer one up to 10 psi (G6).

2. Then, pressurize the inner one up to 40 psi and then the outer one up to 30 psi.

3. And so on until desired outer chamber pressure is reached.

NOTE 1: Too much pressure difference between the inner chamber and the outer chamber may cause damage to the O-ring seals.

NOTE 2: The pressure of the outer chamber (G6) determines the velocity of the striker bar and average strain rate. The pressure of the inner chamber is used to position the internal piston of the air gun.

NOTE 3: It may be that pressurizing the inner chamber may (due to slight leakage) also pressurize the outer chamber. In this case, a 10 psi difference may automatically be achieved without opening the outer chamber nitrogen tank.

NOTE 4: The inner chamber was designed with a 1000 psi limit. The outer chamber was designed with a 3000 psi limit.

NOTE 5: The striker bar should never be fired at a velocity that would induce plastic deformation in the bars. Stress in these bars should never exceed 75% of the quasi-static yield stress (listed as 150 ksi min per AMS 5662) of the Inconel 718 material.

VII. Open the Trigger Valve (T.V.) to Fire the Gun Immediately After the Correct Pressure is Obtained

VIII. Recording Data and Setting Up for Next Test

a. Ensure that both bar 1 and 2 waves are displayed by the oscilloscope and time is displayed by the velocity indicator.

b. Push "store" button to record waves.

c. Record the time displayed by the velocity indicator.

d. Remove and save the specimen.

e. Return to Part III or IV.

IX. Shutting Down at End of Test Session

Relieving the Pressure on the Feed Lines After Firing.

a. Make sure that the T.V. is open. (T.V.=trigger valve v7)

b. Close the main valves on the supply tanks.

c. Open the valve (v6) slowly to relieve the low pressure line completely and close it.

d. Relieve the gas in the high pressure line in a similar manner as in Step C.

e. Relieve the regulator valves.

f. Make sure that the triggering valve (T.V.) is open.

g. Close all other valves except the T.V.

X. References (Kept in Control Room 005A)

Nicolet Manual
Operations Manual - Striker Bar Velocity Timer
SHPB Design Sketches and Misc.

XI. Plotting SHPB Signals from the Nicolet 4094

a. With FUNCTION switch in PEN mode recall track needed from the Nicolet XF-44 storage unit with the memory of the scope in ALL mode. This must be done with storage control of scope on HOLD LAST. If correct wave forms are already stored on scope, ignore the step. **NOTE:** Storage unit must have access door in open position if no disk is in storage unit. Disks should not be left in unit after use.

b. Set MEMORY switch to display only the Bar 1 wave.

c. Place FUNCTION switch on scope to PEN mode.

d. Load paper into plotter.

e. Press the scope EXECUTE button. This will draw the border.

f. Press EXECUTE again. This will print out Bar No. 1 header and Bar No. 1 signal.

g. Set the scope MEMORY position to to Q1 or Q3 to display only transmitted bar wave. This will plot out the Bar No. 2 signal with its header when EXECUTE is pressed again.

h. Press the VIEW button on the plotter and remove the paper.

i. Take the function control from PEN to any other setting to get out of plot mode. This will cause an error "bleep", but this is of no concern. The internal program is for sequentially plotting four channels of data so the execute light will stay green after plotting only two channels. Thus, as stated before, the error bleep is not critical.

XII. Data Analysis

The stored waves are manipulated to extract voltages from the incident, transmitted, and integrated reflected waves. These voltages along with the other data are used by the computer program to calculate the striker bar velocity, the stress and strain calibration constants, and the ultimate stress, strain, and strain rate. The program can also calculate values for the yield stress, strain, and strain rate, and the elastic modulus.

The data analysis process begins with the display on the oscilloscope of the reflected and transmitted waves. As seen on the oscilloscope, wave 1B is the upper transmitted wave and wave 1A is the lower, reflected wave.

Beginning with wave 1B, the first point to find is the zero time reference point. This is the point on the wave at which a linear increase in voltage begins and is not to be confused with the first increase in voltage. The coordinates of the zero time reference point, found by manipulating the cursor keys and the vertical and horizontal expansion knobs, can be annotated on the SHPB Test Data Sheet (Figure 4) or the RESET NUM function can

be used to designate the point as 0 volts, 0 microseconds. Experience has found that it is more convenient to annotate the coordinates of this point on the data sheet because it made re-checking easier.

The next point to find is the transmitted wave voltage at yield (DELVYS). This point is defined as the first break in the wave's linear increase in voltage (Figure 5). The final point to be determined is the transmitted wave voltage at ultimate (DELVUS) which occurs at the maximum voltage of the wave past the elastic region.

The coordinates of each point are recorded in units of volts and microseconds. For calculation purposes all voltages are read as positive. The transmitted wave time to yield or ultimate (DELT) is the difference, in microseconds, between either the DELVYS time measurement or the DELVUS time measurement and the zero time reference point, respectively. The selection of either the DELVYS or DELVUS times determines whether the strain rate at yield or ultimate is calculated.

The reflected wave maximum voltage (DELV1) is determined from wave 1A. Taking the initial horizontal portion of the wave as the zero voltage reference, DELV1 is the maximum voltage of the curve (Figure 5).

With the transmitted and reflected wave data recorded, wave 1A is integrated from its origin to a point that corresponds with any point after DELVUS on 1B. The integration is performed by inserting the Nicolet program disk into one of the disc drives, placing the storage control mode in the LAST position, and recalling program 16. With the LED display showing P16, PROG on the function switch is selected and the Execute button pressed. The program prompts the operator for appropriate input through its execution. It is important that the right endpoint be placed after DELVUS, that the horizontal reference line be at zero voltage, and that the coordinates from wave 1A are used for each point.

The integrated reflected wave will replace the original reflected wave on the display. This wave and the transmitted wave which appears above it should be stored on the next, even track of the data storage disc.

From the integrated wave (Figure 6), three measurements are made. The integrated reflected wave maximum voltage (DELV2) is recorded at the maximum voltage of the wave between the origin and DELVUS. DELV2 is

determined by locating the maximum point on the wave, selecting RESET NUM on the function switch, and reading the voltage on wave 1B in kilovolts. The RESET NUM function is then executed and the coordinates of DELV2 are set at 0 seconds, 0 volts. Placing the function switch in DATA MOVE and recalling the time on the transmitted wave where the yield point occurred, the vertical cursor is moved along the integrated wave to the corresponding time. With the vertical cursor set on the correct time position on wave 1A, the AUTOCENTER switch can be used to quickly and accurately align the horizontal cursor on the wave. RESET NUM is again selected and the voltage on wave 1B is then read and recorded on the test data sheet as DELVYE. DELVUE is found using the same procedure at the DELVUS time.

The test results are calculated by the BASIC computer program SHPB. After it is loaded on an IBM PC or equivalent, the program prompts the user for the data from the data sheet. When all of the data has been entered, the program presents the results on the screen. The results are then copied or printed for further use and integration.

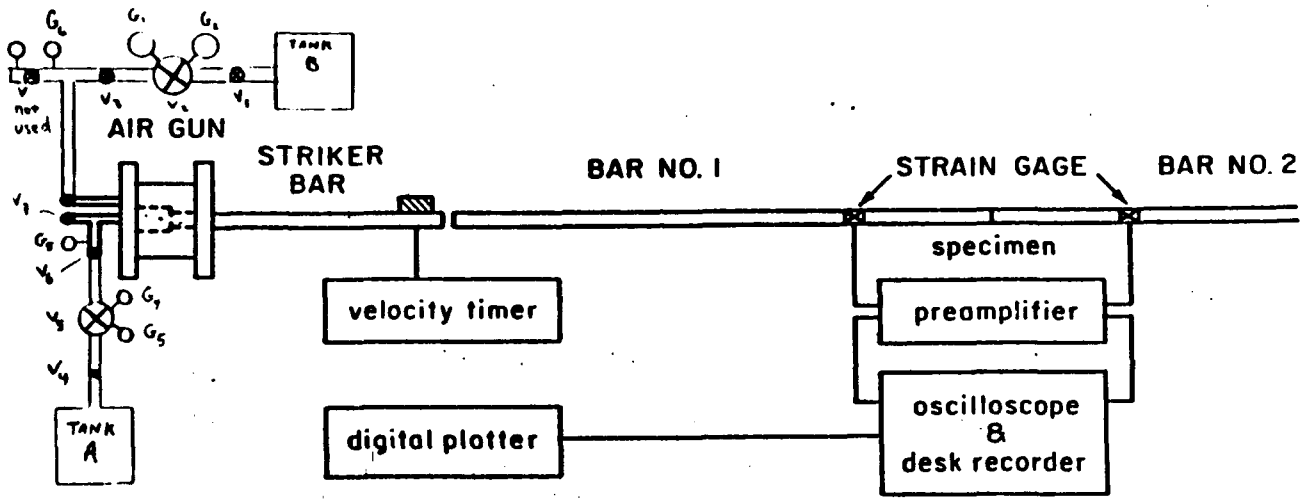

Fig. 1 Schematic view of Split Hopkinson Bar Apparatus

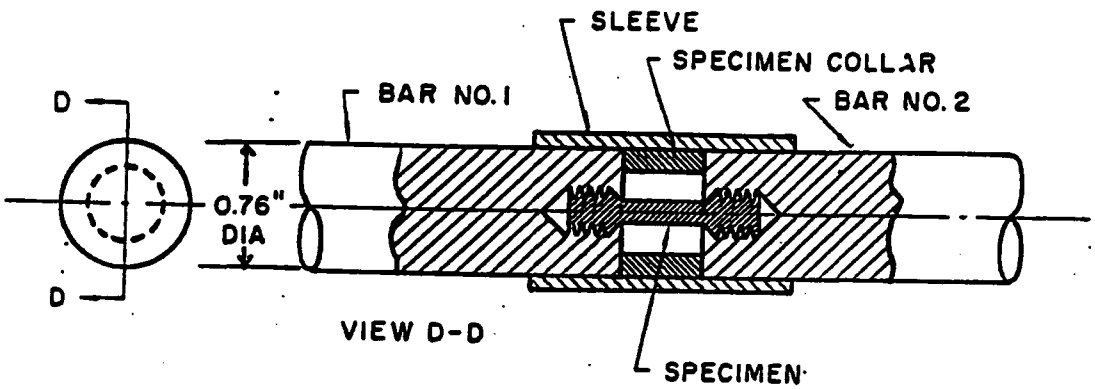

Figure 2. Mounting Tensile Specimen.

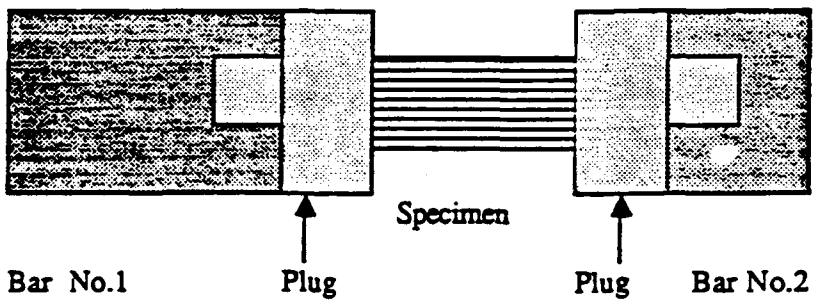

Figure 3. Mounting Compression Specimen.

SHPB Test Data Sheet

I. General

Operator: Parker
Date:
Material: Dimox A
Test: Specimen: Disk:
Temperature: (F)
Pressure: (psi)

II. Raw Data/Computer Input

Specimen Length (XLS): (inch)
Specimen Radius (RS): (inch)
Velocity Indicator (TIME) (microsecond)

Transmitted Wave Voltage @ Yield (DELVYS): (Volt) @ µsec
" " " @ Ult. (DELVUS): (V) @ µsec
" " Time to Ult. or Yield (DELT): (µsec)
Incident Wave Max. Voltage (DELV1): (V)

Integrated Refl. Wave Max. Voltage (DELV2): (kV)
" " " Voltage @ Yield (DELVYE): (kV)
" " " " @ Ult. (DELVUE): (kV)

III. Results

Striker Bar Velocity (VEL): (in/sec)
Stress Calibration Const. (FS): (psi)
Strain " " (FE): (in/in)
Yield Stress (YS) (psi)
Ultimate Stress (US): (psi)
Strain at Yield (YE): (in/in)
Strain at Ultimate (UE): (in/in)
Strain Rate (RATE): (/sec)
Modulus (ES): (psi)

Figure 4. SHPB Test Data Sheet.

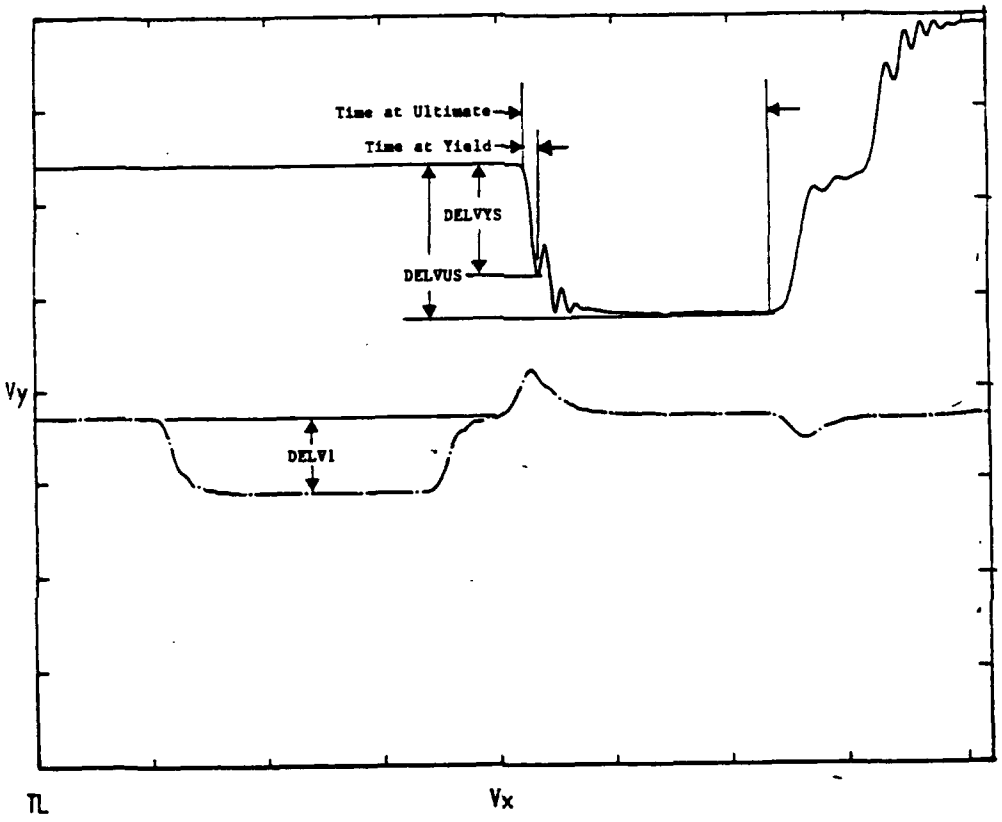

Figure 5. Reflected and Transmitted Waves.

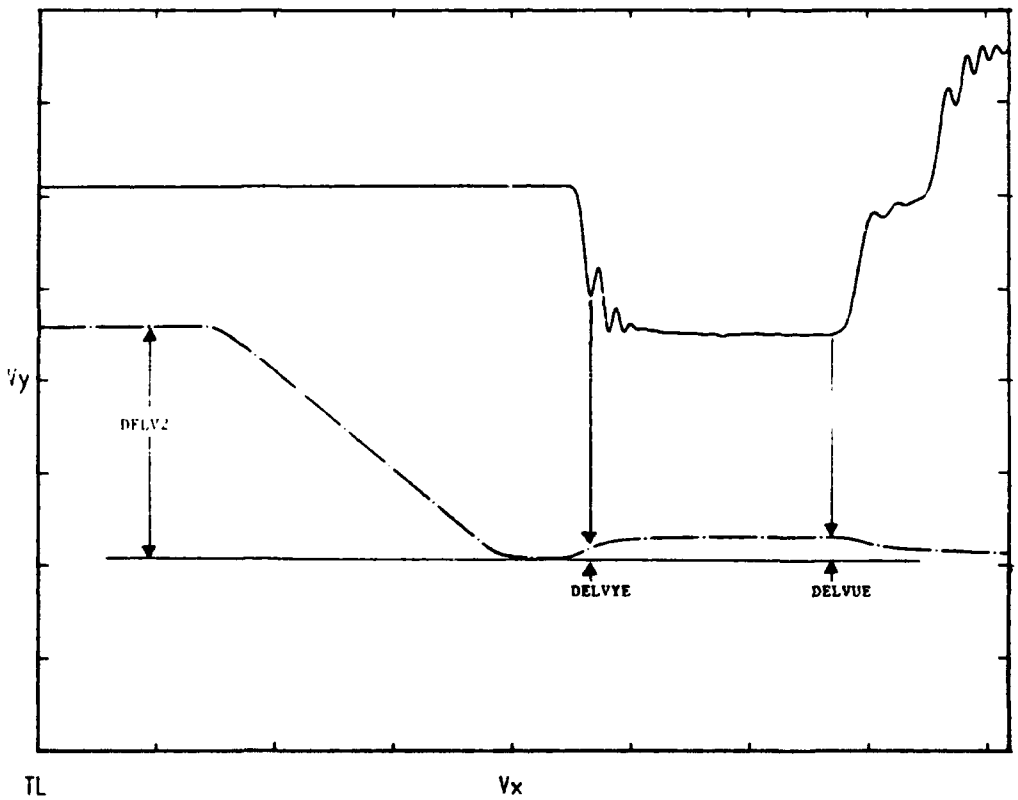

Figure 6. Integrated Reflected and Transmitted Waves.

Appendix B

SHPB COMPUTER PROGRAM

```
100 REM THIS PROGRAM ANALYZES THE DATA FROM THE SHPB
105 REM ALL DATA ENTERED AS EITHER MICROSECONDS, VOLTS, OR INCHES
106 REM EXCEPT DELV2, DELVYE, AND DELVUE WHICH ARE IN KILOVOLTS
110 EB=2.97E+07
120 CB=197000!
130 RB=.375
140 XLSB=28.5
145 INPUT"SPECIMEN DATA";S$
150 INPUT"SPECIMEN LENGTH";XLS
160 INPUT"SPECIMEN RADIUS";RS
170 INPUT"STRIKER BAR TIME";TIME
180 INPUT"TRANSMITTED WAVE VOLTAGE AT YIELD";DELVYS
190 INPUT"TRANSMITTED WAVE VOLTAGE AT ULTIMATE";DELVUS
200 INPUT"TRANSMITTED WAVE TIME TO ULTIMATE";DELT
210 INPUT"REFLECTED WAVE MAX VOLTAGE";DELV1
220 INPUT"INTEGRATED REFLECTED WAVE MAX VOLTAGE";DELV2
230 INPUT"INTEGRATED REFLECTED WAVE VOLTAGE AT YIELD";DELVYE
240 INPUT"INTEGRATED REFLECTED WAVE VOLTAGE AT ULTIMATE";DELVUE
250 REM
260 VEL=4!/(TIME*.000001)
270 FE=(XLSB*2*VEL)/(XLS*CB*DELV2)
280 FS=(EB*RB*RB*VEL)/(RS*RS*2*CB*DELV1)
290 YS=FS*DELVYS
300 US=FS*DELVUS
310 YE=FE*DELVYE
320 UE=FE*DELVUE
330 RATE=UE/(DELT*.000001)
340 ES=YS/YE
345 PRINT S$
350 PRINT"BAR VELOCITY (IN/SEC) = "VEL
360 PRINT"STRESS CALIBRATION = "FS
370 PRINT"STRAIN CALIBRATION = "FE
```

```
380 PRINT"YIELD STRESS (PSI) = "YS
390 PRINT"ULTIMATE STRESS (PSI) = "US
400 PRINT"YIELD STRAIN (IN/IN) = "YE
410 PRINT"ULTIMATE STRAIN (IN/IN) = "UE
420 PRINT"STRAIN RATE (1/SEC) = "RATE
430 PRINT"ELASTIC MODULUS (PSI) = "ES
440 PRINT
450 INPUT"SEND OUTPUT TO PRINTER (Y OR N)";A$
460 IF A$<>"Y" THEN END
470 LPRINT"BAR VELOCITY (IN/SEC) = "VEL
480 LPRINT"STRESS CALIBRATION = "FS
490 LPRINT"STRAIN CALIBRATION = "FE
500 LPRINT"YIELD STRESS (PSI) = "YS
510 LPRINT"ULTIMATE STRESS (PSI) = "US
520 LPRINT"YIELD STRAIN (IN/IN) = "YE
530 LPRINT"ULTIMATE STRAIN (IN/IN) = "UE
540 LPRINT"STRAIN RATE (1/SEC) = "RATE
550 LPRINT"ELASTIC MODULUS (PSI) = "ES
560 PRINT A:SHPB
Ok
```

REFERENCES

[1] Lankford, J. and Gray, W. Composite Armor. In *Concise Encyclopedia of Composite Materials*, Pergamon Press, Oxford, England, 1989.

[2] Lankford, J. Mechanisms Responsible for Strain-rate Dependent Compressive Strength in Ceramic Materials. *Journal of the American Ceramic Society,* 64, 2, 1981.

[3] Lankford, J. Inertia as a Factor in the Dynamic Strength of Brittle Materials. *Journal of the American Ceramic Society,* 65, 8, 1982.

[4] Kipp, M. E., Grady, D. E., and Chen, E. P. Strain-rate Dependent Fracture Initiation. *International Journal of Fracture,* 16, 5, 1980.

[5] Lankford, J. The Role of Sub-Critical Tensile Microfracture Processes in Compression Failure of Ceramics. In *Fracture Mechanics of Ceramics vol. V,* Plenum Press, New York, N. Y., 1983.

[6] Arrowood, R., and Lankford, J. Compressive Fracture Processes in an Alumina-Glass Composite. *Journal of Materials Science*, 22, 10, 1987.

[7] Lankford, J. and Blanchard, C. R. Response of Whisker-Reinforced Ceramic Matrix Composites to Dynamic Compressive Loading. *Materials Science & Engineering A,* A138, 1991.

[8] Lankford, J. Dynamic Compressive Fracture in Fiber-reinforced Ceramic Matrix Composites. *Materials Science & Engineering A,* A107, 1989.

[9] Dormeval, R. The Adiabatic Shear Phenomena. In *Materials at High Strain Rates,* Elsevier Applied Science, London, England, 1987.

[10] Merala, T. B., Chen, H. W., Howitt, D. C., Kelsey, P. V., Korth, G. E., and Williamson, R. L. Dislocation Microstructures in Explosively Deformed Hard Materials. *Materials Science and Engineering A,* A105/106, 1988.

[11] Yeshuran, Y., Rosenberg, Z., and Brandon, D. G. On the Shock-Loaded Two-Phase Ceramics. In *Materials at High Strain Rates,* Elsevier Applied Science, London, England, 1987.

[12] Ruiz, C. Overview of Impact Properties of Monolithic Ceramics. In *Materials at High Strain Rates,* Elsevier Applied Science, London, England, 1987.

[13] Newkirk, M. S., Lesher, H. D., White, D. R., Kennedy, C. R., Urquhart, A. W., and Claar, T. D. Preparation of Lanxide® Ceramic Matrix Composites: Matrix Formation by the Directed Oxidation of Molten Metals. *Ceramic Engineering Science Proceedings,* 8, 1987.

[14] Aghajanian, M. K., Macmillan, N. H., Kennedy, C. R., Luszc, S. J., and Roy, R. Properties and Microstructures of Lanxide® Al_2O_3-Al Ceramic Composite Materials. *Journal of Materials Science,* 24, 1989.

[15] Urquhart, A. W., Molten Metals Sire MMCs, CMCs. *Advanced Materials and Processes,* 7, 1991.

[16] Newkirk, M. S., Urquhart, A. W., Zwicker, H. R., and Breval, E. Formation of Lanxide® Ceramic Composites Materials. *Journal of Materials Research,* 1, 1986.

[17] Kolsky, H. An Investigation of the Mechanical Properties of Materials at Very High Strain Rates of Loading. *Proceedings of the Physical Society, B, 1962.*

[18] Zukas, J. (ed.). *Impact Dynamics.* John Wiley and Sons, New York, N. Y., 1982.

[19] Frey, T. J. *High Strain Rate Effects on Composite Material Properties.* Master's Thesis, Department of Mechanical Engineering, University of Delaware, 1990.

[20] Choe, G. H. *Impact Testing of Composite Materials at High Strain Rates*. Master's Thesis, Department of Mechanical Engineering, University of Delaware, 1989.

[21] Rand, J. L. *An Analysis of the Split-Hopkinson Pressure Bar*. Technical Report NOLTR67-156, United States Naval Ordanance Laboratory, 1967.

[22] Lindhom, U. S., and Yeakley, L. M. High Strain Rate Testing: Tension and Compression. *Experimental Mechanics*, 8, 1, 1986.

[23] Gorham, D. A., Pope, P. H., and Cox, O. Sources of Error in Very High Strain-rate Compression. In *Institute of Physics Conference Series No. 70*, Oxford, England, 1984.

[24] Lindholm, U. S. Some Experiments with the Split-Hopkinson Pressure Bar. *Journal of the Mechanics and Physics of Solids*, 12, 1964.

[25] Hall, I. W. Unpublished Work, 1992.